Strathprints Institutional Repository

Robust Multi-disciplinary Design and Optimisation of a Reusable Launch Vehicle

R. Wuilbercq,* F. Pescetelli,* A. Mogavero,* E. Minisci,† R.E Brown‡

Centre for Future Air-Space Transportation Technology,
University of Strathclyde, 75 Montrose Street, Glasgow G11XJ, United Kingdom

For various technical reasons, no fully reusable launch vehicle has ever been successfully constructed or operated. Nonetheless, a range of reusable hypersonic vehicles is currently being considered as a viable alternative to the expensive but more conventional expendable rocket systems that are currently being used to gain access to space. This paper presents a methodology that has been developed for the rapid and efficient preliminary design of such vehicles. The methodology that is presented uses multi-disciplinary design optimization coupled with an integrated set of reduced-order models to estimate the characteristics of the vehicle's aero-thermodynamic, propulsion, thermal protection and internal system architecture, as well as to estimate its overall mass. In the present work, the methodology has been applied to the multi-disciplinary modelling and optimization of a reusable hybrid rocket- and ramjet-powered launch vehicle during both the ascent and re-entry phases of its mission.

I.   Introduction

$\mathbf{F}$UTURE trans-atmospheric vehicles will, by means of a complex hybrid propulsion system, accelerate up to orbital speed when still within the denser part of the terrestrial atmosphere. The high velocity of the vehicle, when combined with the high air density in the lower atmosphere, will expose it to a severe heating environment. By contrast, during atmospheric entry at very high speeds, the same vehicle will most likely follow an un-powered gliding trajectory during which deceleration to lower velocities will occur at high altitude where the density of the air is relatively low. Although it may be possible to design the vehicle so that the peak heating during descent may be somewhat lower than that experienced during ascent, the integrated heat load that will need to be dissipated or absorbed by the vehicle will not be very much different between the ascent and descent phases of the mission.

Despite the extreme heating conditions to which future space-access vehicles will be exposed, there will be strict emphasis on their full reusability in order to ameliorate their acquisition cost over multiple missions. Part of this strategy will indeed also be to limit costs by reducing the amount of maintenance and refurbishment that is required between flights. Designers will thus, in all likelihood, find themselves forced to employ a new approach to the design of the vehicle's Thermal Protection System (TPS). This will almost certainly result in a switch from the classic insulated aircraft approach *à la* Space Shuttle to the use of a combination of passive, semi-passive, and active TPS.[1] The resulting TPS will likely make use of both lightweight protective materials and a complex Active Cooling System (ACS) involving the re-circulation of a coolant under the most severely heated parts of the structural skin.

Nonetheless, sizing the TPS exclusively for the high-temperature conditions to which the vehicle might be exposed during its mission might not necessarily ensure that the vehicle will meet all of its performance requirements. For instance, future RLVs will be held at their spaceport for a short period of time between flights to fill their cryogenic propellant tanks and to perform maintenance tasks. During these ground-hold operations, the vehicle will be exposed to ambient ground-level temperature, as opposed to the very high temperatures that characterize their in-flight mission profile. Heat transfer from the atmosphere to the TPS

---

*PhD Student, Student Member AIAA
†Lecturer
‡Director and Professor, Senior Member AIAA

will therefore occur at a much lower rate and the materials that cover the cryogenic tanks might then need to be sized to prevent the hazardous formation of ice on the outer surface of the vehicle prior to launch.

This new generation of hypersonic vehicles is also foreseen to make use of hypersonic air-breathing engines, in particular ramjets or scramjets, in order to achieve the performance required for practical attainment of a Single-Stage-To-Orbit (SSTO) capability. Indeed, supersonic combustion is widely accepted to be the most promising alternative to the use of conventional rocket engines in this context. Instead of carrying separate tanks for fuel and oxidizer during take-off, scramjet-powered vehicles will need only to carry the fuel, using atmospheric oxygen for combustion. While air-breathing propulsion systems are characterized by a much higher specific impulse I_{sp} than rockets, scramjets are subject to strong engine-airframe coupling, adding significant complexity to the design of the vehicle.

These various characteristics emphasize the need to generate and employ a very robust methodology in order to design and optimise future trans-atmospheric vehicle configurations efficiently at a system level. An integrated Robust Multi-disciplinary Design Optimisation (R-MDO) procedure must perforce be used and applied for both the ascent and re-entry phases of the vehicle trajectory in order to optimise concurrently the various subsystems to a point where the concept might become technically feasible. This article presents an attempt to define such a general R-MDO methodology. A prototype such methodology is then applied to study the sensitivity of a representative Reusable Launch Vehicle (RLV) configuration (see Fig. 1) to uncertainties and variability in some of its key design parameters.
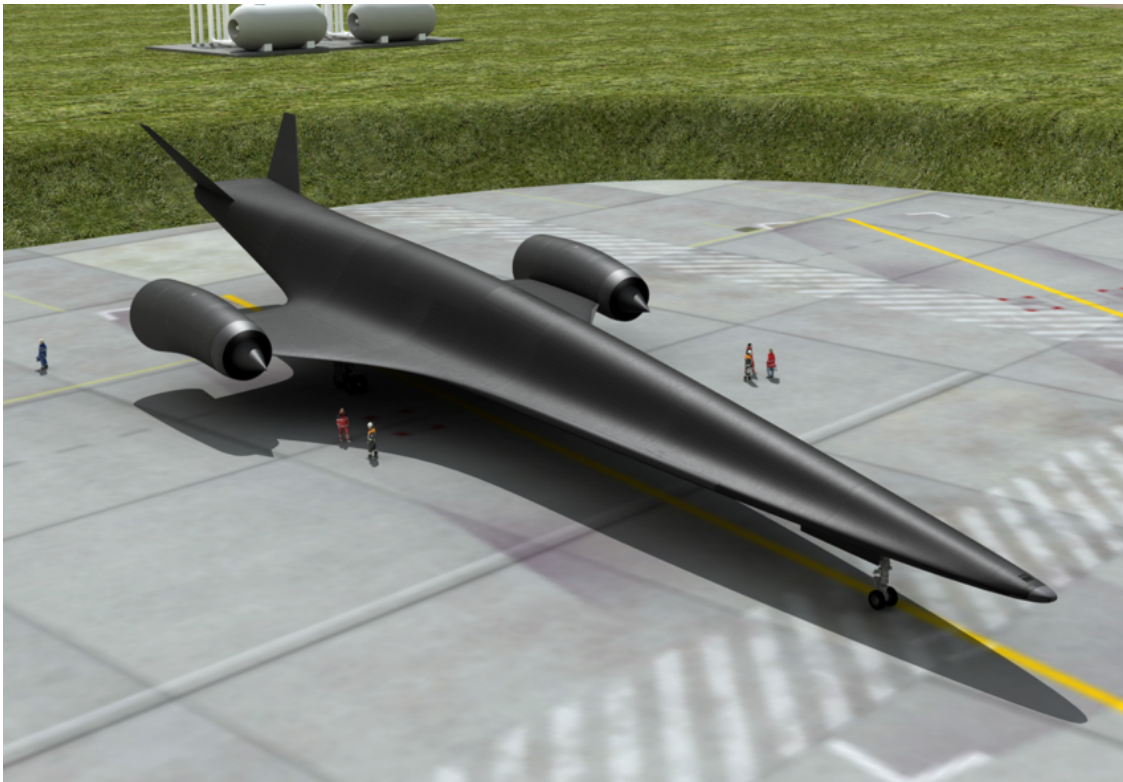

Figure 1: The CFASTT-1 Reusable Launch Vehicle during ground-hold operations. (Original graphic by Adrian Mann.)

II.   System Model

SUCCESSFUL multi-disciplinary design of future trans-atmospheric vehicles will require the development of a system design platform that is itself highly optimized and specialized for the modelling, design and optimization of the hypersonic vehicles to which it will be applied. To be efficient when used for concept exploration, multi-disciplinary optimization or preliminary design, such a platform must emphasize computational efficiency, modularity and accuracy of its performance predictions. The present paper introduces a

American Institute of Aeronautics and Astronautics

prototype for such a dedicated platform, called HyFlow, which is composed of several interrelated modules. These modules evaluate the aero-thermodynamic environment, optimise the performance of the propulsion system, size the protective shield, and finally predict the vehicle mass and trajectory while accounting for inherent uncertainty in the system parameters that are encapsulated within each of its constituent models. In the following sections of this article, each of these modules is described in more detail:

II.A. Earth model

The gravitational acceleration g is assumed to vary with altitude according to an inverse square law

$$g(h) = g_0 \left(\frac{h}{R_E + h} \right)^2 \tag{1}$$

where h denotes the altitude above mean sea level, $R_E = 6375$ km is the mean radius of the Earth, and $g_0 = 9.80665$ m/s^2 is the gravitational acceleration at sea level. The atmospheric characteristics (temperature, pressure, density and speed of sound) follow the 1976 US Standard Atmosphere model up to 1000 km. The effects of wind are not accounted for.

II.B. Trajectory Model

In the present work, the vehicle is modelled dynamically as a point with variable mass flying around a spherical, rotating earth. The translational motion of the vehicle along its trajectory is governed by the following set of differential equations:[3]

$$\dot{h} = v \sin \gamma \tag{2}$$

$$\dot{v} = \frac{F_T \cos \epsilon - D}{m} - g \sin \gamma + \omega_E^2 (R_E + h) \cos \lambda (\sin \gamma \cos \lambda - \cos \gamma \sin \chi \sin \lambda) \tag{3}$$

$$\dot{\gamma} = \frac{F_T \sin \epsilon + L}{mv} \cos \mu - \left(\frac{g}{v} - \frac{v}{R_E + h} \right) \cos \gamma + 2\omega_E \cos \chi \cos \lambda$$
$$+ \; \omega_E^2 \left(\frac{R_E + h}{v} \right) \cos \lambda (\sin \chi \sin \gamma \sin \lambda + \cos \gamma \cos \lambda) \tag{4}$$

$$\dot{\chi} = \frac{F_T \sin \epsilon + L}{mv \cos \gamma} \sin \mu - \left(\frac{v}{R_E + h} \right) \cos \gamma \cos \chi \tan \lambda$$
$$+ \; 2\omega_E (\sin \chi \cos \lambda \tan \gamma - \sin \lambda) - \omega_E^2 \left(\frac{R_E + h}{v \cos \gamma} \right) \cos \lambda \sin \gamma \cos \chi \tag{5}$$

$$\dot{\lambda} = \left(\frac{v}{R_E + h} \right) \cos \gamma \sin \chi \tag{6}$$

$$\dot{\theta}_L = \left(\frac{v}{R_E + h} \right) \frac{\cos \gamma \cos \chi}{\cos \lambda} \tag{7}$$

where v is the speed of the vehicle as measured in an Earth-centred reference frame (assumed to have a rotation rate $\omega_E = 7.2921 \times 10^{-5}$ rad/s). In these equations, γ indicates the flight path angle, χ is the path directional angle, μ is the bank angle, and λ and θ_L denote respectively the latitude and the longitude of the vehicle at time t. The mass of the vehicle is m, F_T is the magnitude of the thrust produced by its engines, and L and D denote the aerodynamic lift and drag forces, respectively. The angle between the thrust vector and the velocity vector is ϵ, and finally $\dot{m}_{fuel}$ is the fuel mass flow rate. During ascent to orbit, the control law for the vehicle governs the angle of attack α, the bank angle μ, and the thrust F_T. Similarly, for the re-entry phase of the mission, the control law governs the angle of attack α, and the bank angle μ. In both cases the vehicle is thus allowed to perform out-of-plane motions.

II.C. Aero-thermal Model

During a typical mission, an RLV will pass from the denser regions of the lower atmosphere, through the upper regions of the terrestrial atmosphere, to the near-vacuum conditions of space, then return again. The aerodynamic regime to which the vehicle is exposed will thus change from continuum flow at lower altitudes

to free-molecular flow at high altitudes, passing through a transitional flow regime in between. The regime in which the vehicle is operating depends on a non-dimensional parameter called the Knudsen number K_n which measures the relative importance of the particulate nature of the gas. The Knudsen number is formally defined as the ratio of the mean free path of the gas, denoted λ_{gas}, through which the vehicle is travelling to an appropriate measure of the dimensions of the vehicle (e.g. the nose radius or mean aerodynamic chord, depending on context). The various flow regimes encountered by an RLV during its mission, as a function of the Knudsen number, are summarized in Table 1.

Flight Regime	Kn Range
Free-Molecular	$Kn \geq 10$
Transitional	$0.01 < Kn < 10$
Continuum	$Kn \leq 0.01$

Table 1: Flight Regimes encountered by an RLV as a function of the Knudsen Number Kn.

II.C.1. *Aero-thermodynamic Environment*

The aero-thermodynamic module in HyFlow uses a combination of independent panel compression methods to predict the aero-thermodynamics of vehicles travelling at supersonic or hypersonic Mach numbers. The model automatically selects the appropriate method based on estimation of the local Knudsen number in conjunction with a topological feature detection technique to discriminate planar from non-planar regions of the flow geometry to switch from modified Newtonian theory to a tangent-wedge or tangent-cone approximation where appropriate. When the estimated Knudsen number lies within the transitional regime, HyFlow use a bridging technique, defaulting to a simple sine-squared law in the absence of a better approximation, to interpolate between the predictions obtained from its free-molecular and continuum-flow models.

HyFlow accounts for viscous effects by calculating the trajectories of the surface streamlines, using these to determine the local Reynolds number and then integrating the skin friction coefficients for compressible turbulent or laminar flow over a flat plate. The Smart-Meador reference temperature method is used for both laminar and turbulent boundary layers.[4] Temperature effects are included by using Sutherland's viscosity law in order to account for the variation of viscosity with temperature, using standard temperature and pressure as the reference values.

HyFlow can evaluate the aero-thermal load at the surface of the vehicle using a technique that is based directly on the flat-plate reference temperature method that is used, as described above, to evaluate the skin friction coefficients. The well-known Reynolds analogy is used to obtain an estimate of the Stanton number, St, and thus the local convective heating rate $\dot{q}_{conv}$. Since the method based on the Reynolds analogy and streamline tracing is inherently invalid at stagnation features within the flow, a mix of methods is employed in practice, making use of a modified version of the Fay-Riddell formula to calculate the convective heating rate for general three-dimensional stagnation features[5] based on the estimation of the local radius of curvature.[6] HyFlow can also be run in fully laminar, fully turbulent, or transitional modes. A simple prediction correlation, based on experimental data for sharp cones at zero angle of attack, and used by Bowcutt *et al.*[7] in their study of hypersonic waveriders, is presently used to predict the onset of laminar-turbulent transition on the surface of the vehicle.

HyFlow is a panel-based implementation which uses an unstructured triangular mesh to describe the geometry of the vehicle being modelled. Piecewise constant surface properties are assumed across the area of each panel and the accuracy of the model thus increases as the number of triangular faces is increased. A moderately coarse mesh is usually employed in order to maintain a relatively good computational efficiency, particularly when using the model in optimization studies, but local mesh refinement can be applied judiciously in sensitive regions of the geometry, such as on highly curved surfaces and near stagnation features, to improve the overall accuracy of the predictions.[8]

II.D. Thermal Protection System Model

When considering the thermal design of a fully reusable hypersonic vehicle, the use of the insulated aircraft approach described in section I on page 1, for instance which was employed to protect the entire surface of the Space Shuttle with semi-reusable ceramic tiles and blanket, is unlikely to be entirely feasible. The

American Institute of Aeronautics and Astronautics

need for light weight and serviceability together with resistance to high temperatures will most likely require that the passive use of lightweight insulation materials be augmented, at least on the most exposed parts of the vehicle (e.g. the leading edge of the wing, and the nose region), by a complex Active Cooling System (ACS) involving the flow of a cryogen (possibly part of the vehicle propellant) through actively cooled surface panels. In this paper, it is assumed that the structural skin of the RLV is itself made of a thermally resilient material and thus that surface insulation is not required in those areas where the surface temperature does not exceed a predetermined threshold. In the process of sizing the TPS, the geometry of the vehicle is first partitioned into a number of self-consistent 'thermal zones': this task is performed automatically by the routines implemented within HyFlow's thermal protection model. Within each of these zones, the convective heating profile on the panel that is most severely heated along the trajectory of the vehicle is used to size the thickness of the insulation layer, or the properties of the active cooling system that is required, as appropriate.
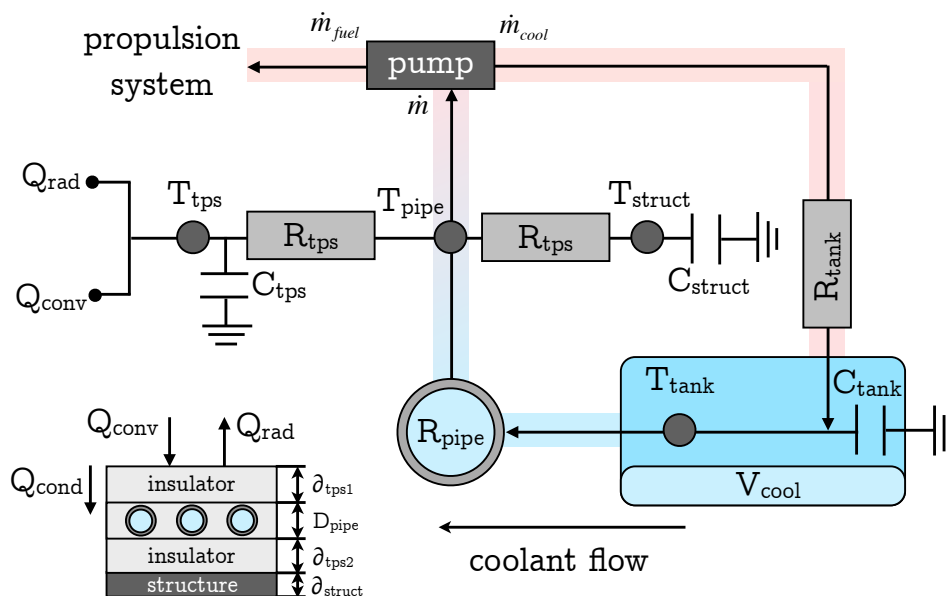

Figure 2: Conceptual thermal network for the Active Cooling System (ACS).

TPS Thermal Network

The schematic of a simplified active thermal management unit and its equivalent thermal network are depicted in Fig. 2. In the present model used within HyFlow, the conductivity of the feeder lines, through which the coolant flows, is neglected on the assumption that they would be made of a thin layer of highly conductive material to enhance the cooling of the most severely heated parts of the aircraft skin. Similarly, the TPS module presently assumes any Reusable Surface Insulation (RSI) to be attached directly to the underlying structural skin of the vehicle, as shown at the bottom left of Fig. 2.

The mass flow rate of cryogen (denoted $\dot{m}_{cool}$ and assumed here to be some of the liquid hydrogen propellant) required to actively cool the vehicle can then be evaluated from the coolant mass flow rate (Eq. 8), which must perforce be designed in order to maintain the structural skin of the vehicle below its prescribed threshold temperature:

$$\dot{m}_{cool} = \rho_{cool} A_{pipe} U_{cool} \tag{8}$$

where ρ_{cool} is the density of the cryogenic fuel, A_{pipe} is the cross-sectional area of the feeder lines, and U_{cool} is the velocity of the pumped coolant flowing through the piping system. Any effects due to boiling of the cryogen within the pipes are neglected at present. The design of the ACS thermal model is aided by adopting a simple electrical resistance analogy where the temperature assigned to a series of nodes within

American Institute of Aeronautics and Astronautics

the system is taken to represent the average temperature of the associated sub-volume of the system (see Fig. 3). Similarly, the (thermal) capacitance assigned to any node is computed from the material properties evaluated at the temperature of the node and is assumed to be concentrated at the nodal centre of the sub-volume.[9]
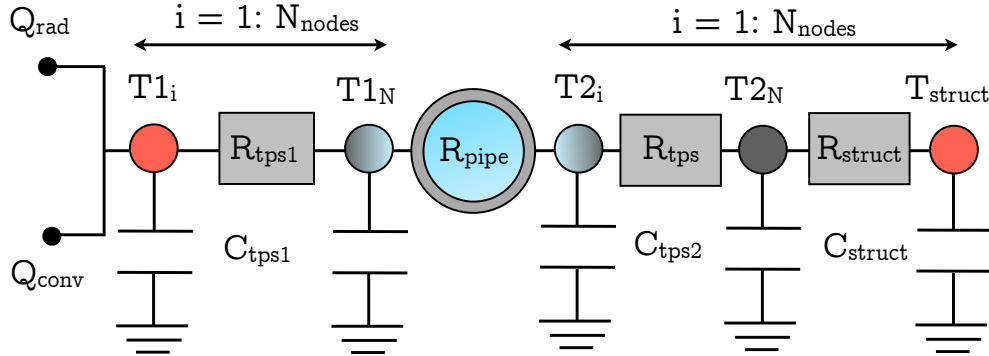

Figure 3: Schematic of the TPS thermal network.

The node T_{1i} in Fig. 3, is assumed to be directly exposed to the external flow; the temperature here is thus dependent on the convective heating from the flow at the surface of the vehicle and the radiative cooling of the surface of the vehicle during its passage through the terrestrial atmosphere. These effects are modelled as external power sources to the thermal network as

$$Q_{conv} = \dot{q}_{conv} A_i \tag{9}$$

and

$$Q_{rad} = \epsilon_{tps} \sigma A_i T_1^4 \tag{10}$$

where A_i represents the surface area of the thermal zone being sized, $\dot{q}_{conv}(t)$ represents the convective heat transfer profile experienced by the thermal zone along the vehicle trajectory, and ϵ_{tps} and σ are, respectively, the emissivity of the surface coating and the Stefan-Boltzmann constant. The various sub-volumes that comprise the entire TPS can be modelled by defining an arbitrary number of material nodes, N_{nodes}, each of which are assumed to have a (thermal) capacitance

$$C_i = \rho_i c_i V_i \tag{11}$$

where the density and specific heat of the TPS material (or fluid) are, respectively, ρ_i and c_i, and V_i is the volume of material available to absorb the thermal load. Each layer of TPS is also assumed to be made out of a material whose conductivity is k_i. As pictured in Fig. 3, in the present study, two protective layers, of thickness δ_1 and δ_2 respectively, have been located on either side of the ACS feeder lines. The last node of the first layer and the first node of the second layer of TPS are indeed considered to be in direct contact with the ACS feeder lines over an equivalent area that here is simply assumed to be equal to the surface area A_i of the thermal zone under consideration. Finally, the set of feeder lines underneath the first TPS layer is modelled as an equivalent convective resistance

$$R_{pipe} = 1/(h_{fuel} A_i) \tag{12}$$

where h_{fuel} is the convective heat transfer coefficient, thus allowing the cooling of the TPS by the forced convection of the pumped cryogen within the pipe to be accounted for. An appropriate empirical formula,[9] depending on the nature of the flow (i.e. on whether it is laminar or turbulent), is used to obtain the forced convective heat transfer coefficient of the coolant. Finally, by application of a thermal energy balance, where the energy flowing into each node must equal the sum of the heat flowing out together with the amount of thermal energy stored at each node, the time evolution of the nodal temperatures within the prescribed ACS scheme can be obtained. After selection of the various materials to be employed within the TPS, a combination of parameters such as the mass flow rate $\dot{m}_{fuel}$, the pipe hydraulic diameter D_{pipe}, and the thicknesses of the RSI layers δ_i must perforce be designed to prevent the structural temperature from rising above a predetermined threshold temperature in order to maintain the structural integrity of the system.
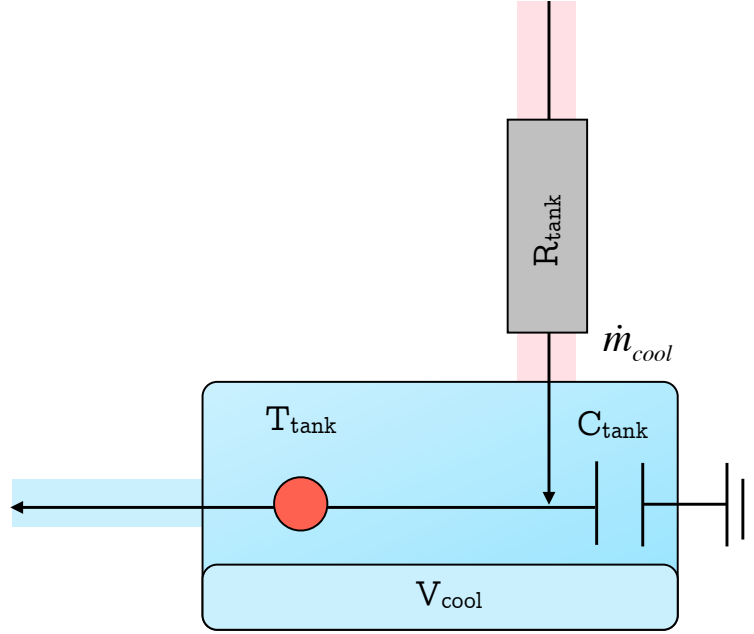
American Institute of Aeronautics and Astronautics

Figure 4: Thermal energy balance at the cryogenic tank.

It is assumed that, during the ascent of the vehicle, any cryogen that is used within the ACS will be sent directly to the propulsion system where it will be mixed with the main fuel supply and fed into the engines. No other provision thus has to be made to store or dissipate the energy that is extracted from the TPS during this phase of the mission. During re-entry, the situation is more difficult, since some means must be found to absorb or dissipate within the system the energy that is absorbed by the ACS. In the present work, it is assumed that a residual amount of propellant has been held within the main fuel tanks with the express purpose of using it within the ACS during re-entry. The cryogen is thus re-circulated to the tank after use within the ACS, where its thermal energy is dissipated firstly by increasing the temperature of the fluid within the tank and subsequently, once the boiling point of the fluid is reached, by vaporising the contents of the tank. In the present work, the re-circulation of the cryogenic fuel through the tank during re-entry has been accounted for by modelling a thermal network for the tank system (see Fig. 4). This network is then coupled to that for the TPS described in the previous section. The thermal resistance

$$R_{tank} = \frac{1}{\dot{m}_{cool} c_{cool}} \tag{13}$$

models the mass flow rate of cryogen that re-circulates from the cooling pipes into the tank, where c_{cool} is the specific heat of the coolant. A differential equation governing the variation of the fuel temperature within the cryogenic tank, denoted T_{tank}, as a result of this heated coolant being returned to the tank can therefore be obtained using the following energy balance:

$$Q_{in,tank} = Q_{stored,tank}$$

in other words

$$\dot{T}_{tank} = \begin{cases} \dot{m}_{cool} c_{cool} \left(\frac{T_{pipe} - T_{tank}}{C_{tank}} \right) & \text{if} \quad T_{tank} < T_{liq} \text{ and } V_{tank} > 0 \\ 0 & \text{if} \quad T_{tank} \geq T_{liq} \text{ and } V_{tank} > 0 \\ \infty \text{ otherwise} \end{cases} \tag{14}$$

where

$$C_{tank} = \rho_{cool} c_{cool} V_{tank} \tag{15}$$

is the capacitance of the tank, with V_{tank} being the total volume of fuel within the tank. The logic within Eq. 14 is required to account for the possibility that the propellant in the tank might boil. Indeed, the

volume of fuel within the tank, denoted V_{tank}, is assumed to vary with time during ascent as the on-board fuel is consumed, and during re-entry as the coolant boils off, according to

$$\dot{V}_{tank} = \begin{cases} -\dot{m}_{fuel}/\rho_{fuel} & \text{during ascent} \\ -\dot{m}_{boil} & \text{during re-entry} \end{cases} \tag{16}$$

where $\dot{m}_{boil}$ is the fuel boil-off rate, and is defined simply as

$$\dot{m}_{boil} = \begin{cases} 0 & \text{if} \quad T_{tank} < T_{liq} \\ Q_{in}/(\Delta H_{fuel}\,\rho_{fuel}) & \text{if} \quad T_{tank} \geq T_{liq} \end{cases} \tag{17}$$

where ΔH_{fuel} represents the latent heat of vaporization of the fuel, evaluated at the pressure that exists within the tank. Indeed, if the fuel inside the tank is warmed to the extent that it reaches its vapour-liquid phase equilibrium (liquefaction) temperature T_{liq} at the corresponding pressure within the fuel system, then the temperature of the fuel does not continue to rise until all the fuel has changed from a liquid to a vapour.
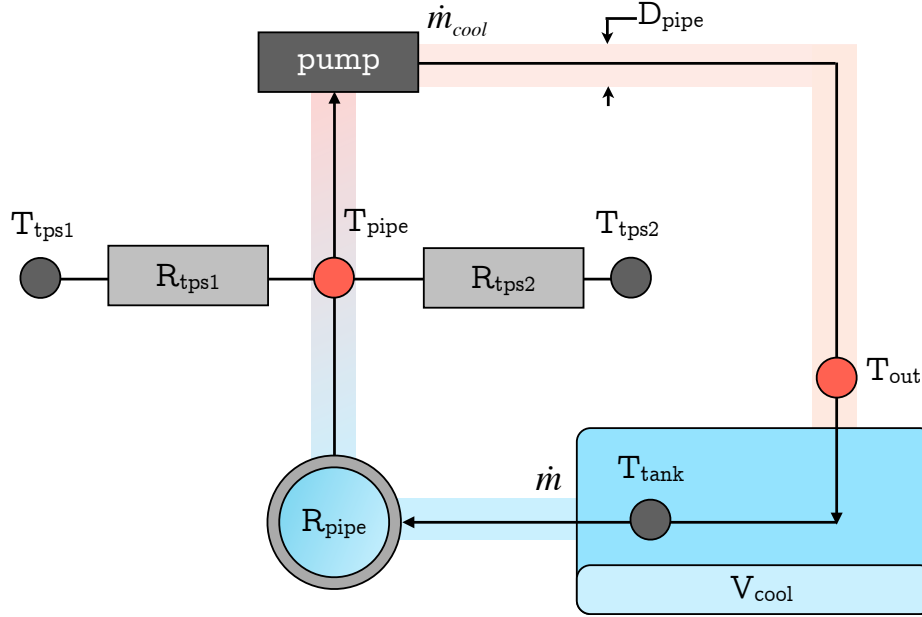
Pipe Node

Figure 5: Thermal energy balance at the pipe node.

The heat input into each section of the ACS feeder lines is a result of the heat conducted from the wall and absorbed by the cryogen, and is given by

$$Q_{in,pipe} = \frac{T_{tps1} - T_{pipe}}{R_{tps1}} \tag{18}$$

Additionally, the heat leaving each section of the pipe is computed as

$$Q_{out,pipe} = \frac{T_{pipe} - T_{tps2}}{R_{tps2}} + \dot{m}_{cool}c_{cool}(T_{out} - T_{tank}) \tag{19}$$

where T_{out} is the temperature of the fluid leaving the feeder lines, and the temperature T_{pipe} of the fluid within the feeder lines is set as the average temperature between the inlet and outlet of the system, i.e.

$$T_{pipe} = \frac{T_{out} + T_{tank}}{2} \tag{20}$$

American Institute of Aeronautics and Astronautics

An energy balance at the pipe node allows the temperature inside the coolant feeder lines to be estimated as:

$$T_{pipe} = \left(\frac{2\dot{m}_{cool} \times R_{eq1} \times R_{eq2} \times T_{tank} + R_{eq1} \times T_{tps2} + R_{eq2} \times T_{tps1}}{2\dot{m}_{cool} \times R_{eq1} \times R_{eq2} + R_{eq1} + R_{eq2}} \right) \tag{21}$$

where R_{eq1} and R_{eq2} are the sum of the convective resistance of the feeder lines and the conductive resistance of the layers of insulation, i.e. TPS1 or TPS2, respectively.

Ground-Hold Analysis

In addition to the problem posed by the extreme heating environment to which the vehicle is subjected during re-entry, the present work also considers the necessity of avoiding the generation of ice at the surface of the vehicle during ground-hold operations between successive missions.
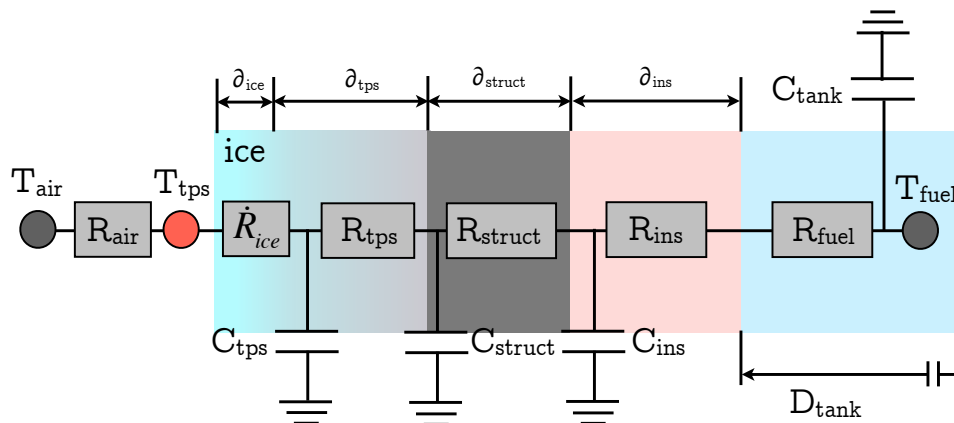

Figure 6: State of the TPS during ground-hold operations.

Indeed, the fuel inside the cryogenic tank will be maintained at a very low temperature before launch (20.4 K for liquid hydrogen, 90.2 K for liquid oxygen); heat will therefore be extracted from the tank structure as well as from the TPS materials that are directly in contact with it, causing temperatures to decrease throughout. If the temperature of the outer surface of the TPS, T_{wall}, decreases below the freezing point of water in the ambient atmosphere ($T_{ice} = 274.15K$ under sea level conditions), for instance during adverse weather conditions or when humidity levels in the atmosphere are high, then the surface of the vehicle could develop a layer of ice prior to launch. The presence of ice on the surface of the vehicle during operations carries with it the potential to be extremely hazardous, and could lead to serious damage to the thermal shield of the RLV as well as increasing the vehicle's mass and potentially reducing its aerodynamic performance. Consequently, it must be ensured that the TPS, especially on those parts of the vehicle that are in close thermal contact with the cryogenic tanks and their insulation, is designed as far as possible to prevent the formation of an ice layer on the surface of the vehicle. It is indeed very important to ensure that the overall optimal TPS thickness does not only satisfy in-flight aero-thermodynamic heating constraints, but is also robust to other considerations that, somewhat ironically given past experience, have traditionally been regarded as of secondary importance during the preliminary design phase.

The problem of calculating the performance of the TPS during ground-hold operations is represented by the simplified thermal network shown in Fig. 6. On the ground, the vehicle is exposed to humid air at the ambient temperature The time evolution of the wall temperature, T_{wall}, can be obtained via a simple energy balance as described below:

Thermal Balance

If the heat input at the wall is assumed to be due to the natural convection of the atmospheric air (e.g.

neglecting solar radiation, for instance), then

$$Q_{in} = \frac{T_{air} - T_{wall}}{R_{air}} \tag{22}$$

The convective resistance R_{air} is given by

$$R_{tps} = \frac{1}{h_{air} A_i} \tag{23}$$

(where the convective heat transfer coefficient for still air, $h_{air} \approx 5.6785$ W/m^2 K under standard sea-level atmospheric conditions where $T_{air} \approx 293.15$ K). Then, the thermal energy that leaves the surface due to the combined effects of conduction through the layer of ice, the TPS, the structural skin and the tank insulation layer, and heat transfer from the tank due to natural convection, can be computed as:

$$Q_{out} = \frac{T_{wall} - T_{fuel}}{R_{eq}} \tag{24}$$

where T_{fuel} represents the temperature of the cryogenic fuel, and the equivalent resistor,

$$R_{eq} = \frac{\delta_{ice}(t)}{k_{ice} A_i} + \frac{\delta_{tps}}{k_{tps} A_i} + \frac{\delta_{struct}}{k_{struct} A_i} + \frac{\ln\left(1 + 2\delta_{ins}/D_{tank}\right)}{k_{ins} \pi D_{tank}} + \frac{1}{h_{fuel} A_{tank}} \tag{25}$$

where D_{tank}, δ_{ice}, δ_{tps}, δ_{struct} and δ_{ins} are, respectively, the diameter of the tank, the thickness of the ice layer with conductivity k_{ice}, the thickness of the TPS layer with conductivity k_{tps}, the thickness of the underlying structural skin with conductivity k_{struct}, and the thickness of the tankage insulation layer with conductivity k_{ins}. The term h_{fuel} represents the natural convective heat transfer coefficient of the fuel, and is based on empirical formulas. Finally, it is assumed that the TPS layer has a thermal capacity, denoted C_{tps}, obtained using Eq. 11 on page 6. The differential equation governing the time evolution of the wall temperature during ground-hold operations can thus be written as

$$\dot{T}_{wall} = \frac{T_{air} - T_{wall}}{R_{air} C_{tps}} + \frac{T_{fuel} - T_{wall}}{R_{eq} C_{tps}} \tag{26}$$

Finally, the rate of growth of the layer of ice on the surface of the vehicle can be modelled as

$$\dot{\delta}_{ice} = \frac{Q_{in}}{\Delta H_f^0 \times \rho_{ice}} \tag{27}$$

where Q_{in} is the heat flux through the layer of ice, ΔH_f^0 is the heat of formation of ice from a vapour, and ρ_{ice} is the density of ice which can vary with the temperature at the surface of the vehicle.
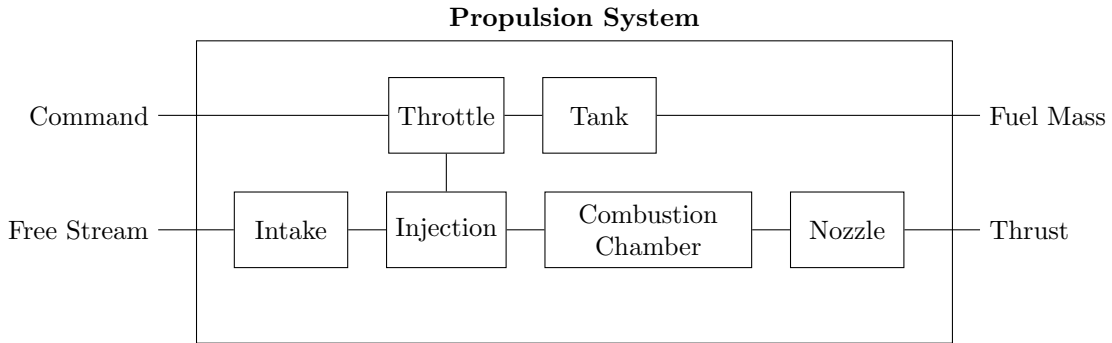
Propulsion System

Figure 7: Example of the modular structure of the propulsion model for a Scramjet/Ramjet.

II.E. Propulsion Model

The propulsion model within the HyFlow platform, called HPPMM (Hybrid Propulsion Parametric and Modular Model), has been developed using the Matlab® programming language. The software has a structure that takes advantage of the intrinsic modularity of the object oriented programming formalism embodied

American Institute of Aeronautics and Astronautics

within the Matlab® environment. This modularity brings significant flexibility to the software by allowing it to be configured to easily model many different kinds of propulsion systems. Moreover, thanks to the object oriented structure of the software, it is possible to implement every module in terms of a defined set of properties and parameters that can be changed easily during run-time. This latter feature makes the software particularly suitable for application to vehicle optimization studies.

In Fig. 7 on the previous page for instance, a schematic of the HPPMM model, structured in order to represent a scramjet/ramjet engine, is depicted. The modules can easily be changed and re-arranged to represent an alternative engine configuration. Hybrid engines can be modelled by collating and interconnecting all the required modules, then switching on/off certain of the modules according to a proposed schedule of operation. Specific details of the models used to calculate the gas dynamics within each of the modules, and thus the overall engine performance, are given by Mogavero *et al.*[17]

The propulsion system of the RLV that is the subject of this particular article is a Rocket Based Combined Cycle (RBCC) engine system, derived from the engine that was proposed for Hyperion, a launch vehicle conceived by the Aerospace Systems Design Laboratory at Georgia Tech.[18] This engine can operate over a wide range of flight conditions by changing its configuration to allow operation in one of several different modes:

- Ejector mode

- Pure ramjet mode

- Pure rocket mode

The ejector mode involves the use of an air-augmented rocket with post-combustor. The engine, when in this mode, is able to provide thrust from subsonic to low supersonic flight conditions with higher specific impulse than a conventional rocket. Once sufficient speed is attained, the rocket can be turned off in order to take advantage of the higher specific impulse of the ramjet mode. The pure rocket mode is eventually employed to provide the final boost for orbital insertion, and is adopted once the thermal limits of the ramjet are reached and the atmosphere becomes too rarefied to sustain air-breathing propulsion. A schematic of the HPPMM model for this propulsion system is depicted in Figs. 8, 9 and 10. In Table 2 the sectional areas of the engines at the conjunctions between the various modules are listed. Both the intake and the nozzle have variable geometry in order to allow the engine to adapt to its wide operational range: the table lists the maximum and minimum areas that these parts of the engine can adjust to during operation. The HPPMM propulsion module allows full control over the switching between the three propulsion modes of the engine. In the present model, the switching between modes is governed simply by the free stream conditions, in particular the Mach number and the total pressure, as delimited by the operational range for the engine in each of its modes as listed in Table 3. As can be seen, the operational ranges of the engine in its various modes overlap to some extent; the switching algorithm thus selects the appropriate mode by giving priority to the mode that is already in operation. In this way, unrealistic cycling between engine modes, particularly near the operational threshold of a particular mode, is avoided in the model.
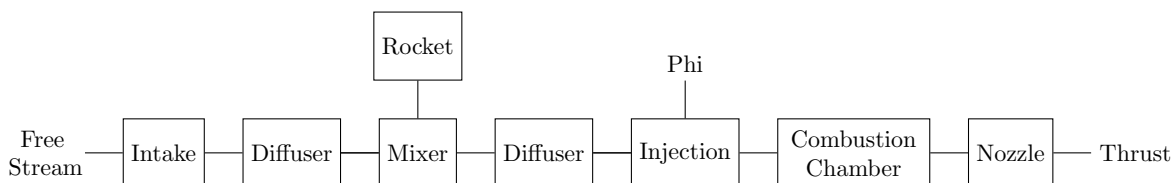

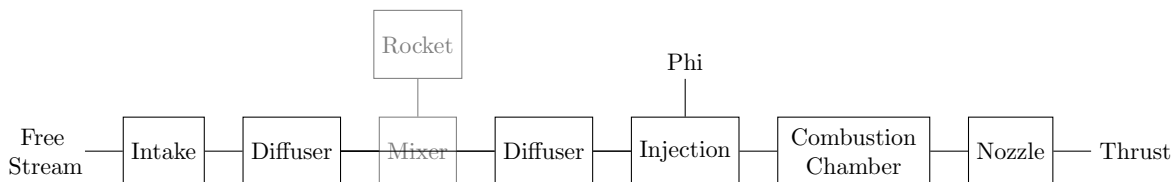**Figure 8:** HPPMM model of the Hyperion engine: ejector mode.

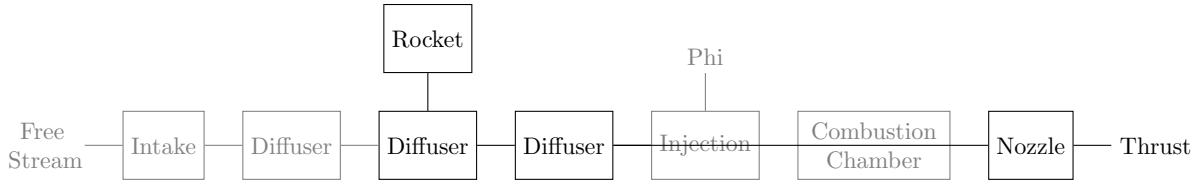**Figure 9:** HPPMM model of the Hyperion engine: pure ramjet mode.

American Institute of Aeronautics and Astronautics

Figure 10: HPPMM model of the Hyperion engine: pure rocket mode.

| | Area [m^2] | |
Node name	Min	Max
Pre-Intake	0	∞
Intake	0	2.5084
Throat	0	0.6271
Pinch Point	0.7655	0.7655
Primary	1.0452	1.0452
Mixer End	1.0452	1.0452
Rocket Outlet	0.2796	0.2796
End Diffuser	2.0903	2.0903
Injection	2.0903	2.0903
End Chamber	2.0903	2.0903
Nozzle	0	8.8258

Table 2: Nodal areas within the HPPMM model of the Hyperion engine.

| | Mach Number | | $p_0[Pa]$ | |
Mode	Min	Max	Min	Max
Ejector Mode	0	3.0	$1 \cdot 10^4$	∞
Pure Ramjet Mode	2.5	8.0	$5 \cdot 10^5$	∞
Pure Rocket Mode	0	∞	0	∞

Table 3: HPPMM model of the Hyperion engine: operating ranges for each propulsion mode.

II.F. Weight Model

The weight model within HyFlow allows the mass of each individual component of the vehicle to be estimated once its flight performance, the dimensions and shape of its subsystems, and the amount of cryogenic fuel required for both the propulsion system and its ACS is known. In the present version of the module, elements of the Hypersonic Aerospace Sizing Analysis (HASA) method have been used in order to estimate the Gross Take-Off Mass (GTOM) of the vehicle. The HASA method is a statistical weight approximation technique, and, despite its lack of accuracy in the evaluation of system mass at component level, it has been shown to approximate correctly the GTOM for various types of hypersonic vehicles, including the Space Shuttle.[10] The weight model within HyFlow can also compute the shift of the location of the centre of mass of the vehicle as the on-board fuel is consumed: this is an important consideration when the longitudinal stability and controllability of the vehicle is being assessed.

II.F.1. Thermal Insulation

The total mass of the TPS can be evaluated as the sum of the masses of the RSI layers applied to the vehicle's surface together with the mass of the ACS, if employed. The mass of an RSI layer is given simply by

$$m_{rsi} = \rho_m A_i \delta_i \tag{28}$$

American Institute of Aeronautics and Astronautics

where δ_i is the thickness of the RSI material, A_i represents the surface area covered by the RSI in the corresponding thermal zone, and ρ_m is the density of the insulation material. Similarly, the mass of the ACS is approximated as the sum of the masses of its component layers of RSI, calculated using Eq. 28 on the preceding page, a basic system mass m_{acs}^0, a term proportional to the length of piping used within the system, and the total mass of coolant, m_{cool}, that passes through the system during the mission:

$$m_{acs} = \sum_{i=1,2} \rho_m A \delta_i + m_{acs}^0 + k_{acs} L_{pipe} N_{pipe} + \int_0^{t_f} \dot{m}_{cool} dt \tag{29}$$

II.F.2. Propulsion System

In the present weight model, the total mass of the propulsion system is considered to be the sum of the mass of the thrust structure m_{thrust} that supports the engines, the mass of the propulsion system itself, denoted $m_{engines}$, and the mass of the fuel required by the propulsion system during the mission, denoted m_{fuel}. The equations for calculating these values within HyFlow are taken directly from the HASA method where m_{thrust} is assumed to scale with the maximum thrust that can be produced by the engines, and $m_{engines}$ is based on a characteristic length of the engine, and the number of engines.

II.F.3. Packaging

The packaging module within HyFlow is responsible for the arrangement of the various system components within the internal space of the vehicle. The internal arrangement can be based on an order that is pre-defined by the user, or can be automatically set to maximize the forward location of the centre of mass of the vehicle for considerations of longitudinal stability. Additionally, the packaging module provides a means of verifying that all of the internal components, such as the tanks, subsystems and payload can be accommodated within the Inner Mould Line (IML) of the vehicle. The IML is obtained by offsetting the external mesh of the vehicle by the local TPS thickness. If the internal configuration of the vehicle does not fit within the boundaries defined by the IML, the module then automatically scales the vehicle so that it does.

III. Baseline Trajectory

THE selection of an appropriate set of optimisation tools for the design of vehicle trajectories is never a particularly straightforward process. The convergence of conventional, simple gradient-based optimisation routines is often severely hampered by particular features that are embedded within the model for the system's performance. Changes in behavioral mode or other discontinuities embedded within the model cause particular problems in this respect. The choice of optimisation algorithm can thus influence the outcome of the design process considerably, and it can be difficult, if not impossible, to find the true, globally-optimal design solution even if a good initial guess is available. The method used in the present work is based on a mixed approach. A population-based stochastic algorithm is used first to explore the design space and to identify a set of neighbourhoods in which candidates for the global optimum of the system might exist. A gradient-based approach is then used in each such neighbourhood to refine the solution and to ensure that the constraints on the system are accurately met.[13] Following this, the highest ranked solution according to its cost function is accepted as the global optimum. To optimise the re-entry trajectory of our representative RLV, a direct collocation method based on the Finite Elements in Time (FET) approach and using a spectral basis[12] is applied: in this approach, the trajectory is discretised into a large but finite number N of sub-intervals, and the design space is then the matrix product of the unit vector of dimension N and a suitable control vector c for the vehicle along its trajectory. The resultant non-linear programming (NLP) problem[14] is then solved using the MOPED[15] algorithm to search for candidate optima; these solutions are then refined using the gradient-based IDEA[16] optimisation method.

III.A. Ascent trajectory

To obtain the ascent trajectory for our representative RLV, the control vector c is given by the variation of the angle of attack α, the bank angle μ and the throttle control δ_T (and hence the engine thrust F_T) along the
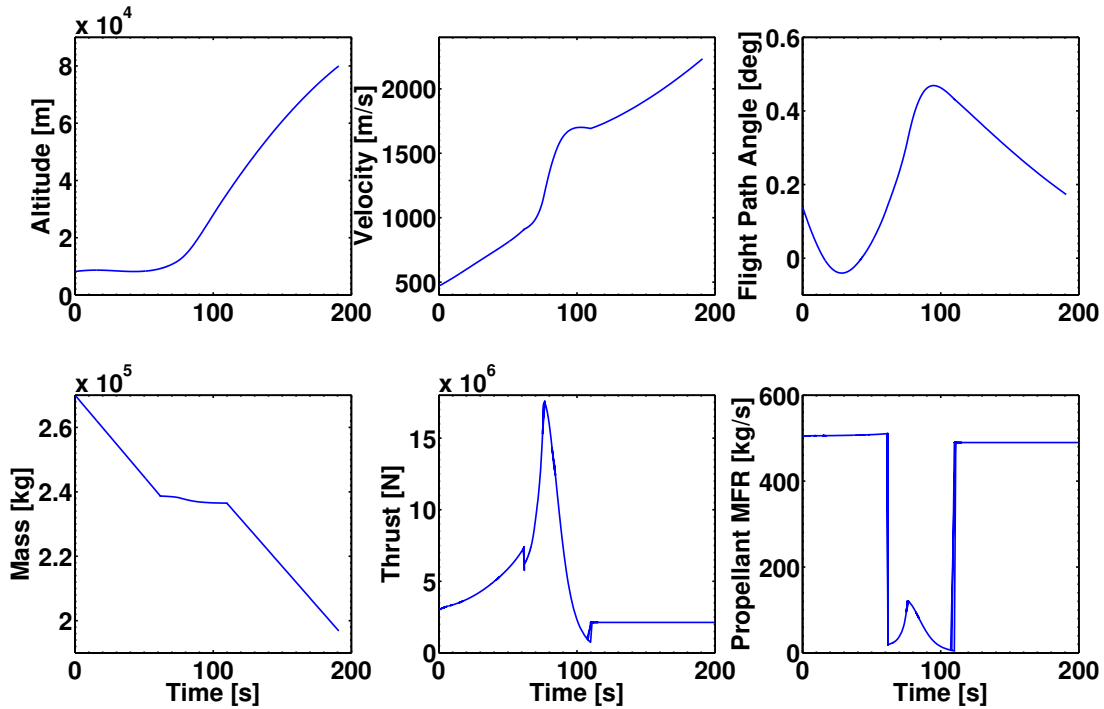
Figure 11: Baseline ascent trajectory for the CFASTT-1 vehicle.

trajectory. The optimal control problem[13] aims to maximize the payload mass on board our representative RLV, i.e. to find

$$\max_{\mathbf{c} \in D} \ m_{pay} \tag{30}$$

subject to the dynamics described in Section II.B on page 3 and initial conditions (i.e. at $t = 0$) $h_0 = 8.2$ km, $v_0 = 0.470$ km/s, $\gamma_0 = 8°$, $\chi_0 = 0°$, $\lambda_0 = 0°$, $\theta_{L0} = 0°$ set to start after the transition into the supersonic regime. The terminal conditions (i.e. at $t = t_f$) are $h_f = 80$ km, $v_f = 8.2$ km/s, and $\gamma_f = 0.2°$ are those required to enter into a circular orbit at 80 km altitude. Path constraints are imposed on both the peak heat flux at the nose stagnation point, $\dot{q}$ and the dynamic pressure q_∞, as well as on the normal and axial accelerations, a_y and a_z experienced by the vehicle. The resultant baseline trajectory for the ascent into orbit is shown in Fig. 11.

III.B.   Re-entry trajectory

During the subsequent re-entry, the RLV follows an un-powered, gliding trajectory controlled by the angle of attack α and the bank angle μ. The nominal control law $c(t)$ is then obtained as the solution of the optimisation problem which aims to minimize the integrated heat load at the nose stagnation point:[11]

$$\min_{\mathbf{c} \in D} \int_{t_0}^{t_f} \dot{q}_{st}(t)dt \tag{31}$$

subject to the dynamics described in Section II.B on page 3 and initial conditions (i.e. at $t = 0$) set to start in the hypersonic regime: $h_0 = 120$ km, $v_0 = 7.8$ km/s, $\gamma_0 = -1°$, $\chi_0 = 90°$, $\lambda_0 = 1°$, $\theta_{L0} = 0°$. The terminal conditions (i.e. at $t = t_f$) are $h_f = 24$ km, $v_f = 0.8$ km/s, $\gamma_f = -30°$, $\chi_f = 90°$, $\lambda_f = 40°$, and $\theta_{Lf} = 0°$. Additional path constraints are imposed on the peak heat-flux at the nose stagnation point $\dot{q} < 500,000$ W/m^2, and the maximum acceleration along the normal body axis so that $a_y(t) \leq 28$ m/s^2. The resultant baseline trajectory for the descent of the vehicle into the terrestrial atmosphere is shown in Fig. 12 on the following page.
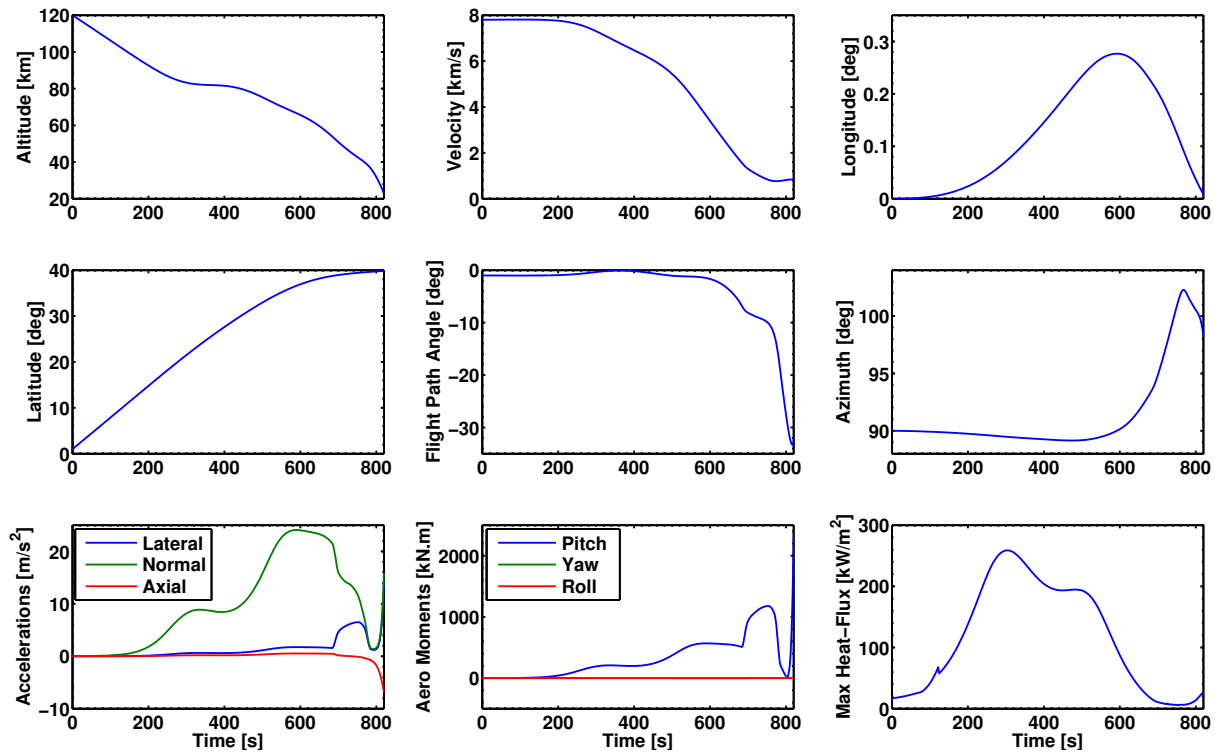
Figure 12: Baseline re-entry trajectory for the CFASTT-1 vehicle.

IV. Design Analysis

DUE to the strong coupling between its various subsystems (e.g. the propulsion system and the airframe structure and aerodynamics, as mentioned earlier), the task of designing an RLV is inherently multi-disciplinary: many of the design variables have a considerable mutual influence, and design objectives and constraints can be mutually conflicting to an extent which is amplified by the extremely tight tolerances on vehicle performance that need to be achieved. It becomes essential thus to be able to quantify, as early on in the design process as is possible, the effects of uncertainty in some of the key design variables in order to provide reliable estimates of the margins on the likely performance of the vehicle. The advantage of the use of a low-order but comprehensive parametric model for preliminary design, such as the HyFlow system that was introduced in section II on page 2, is of course the ease with which parametric variations in the properties of the vehicle system can be explored.

Two fundamentally different types of uncertainty are inherent to the system. The first type is the *stochastic* uncertainty (also called random uncertainty) that is associated with inherent variations in the physical system or its environment. An example would be the natural variability in the properties of the material used to construct the layers of TPS on the vehicle, or the natural fluctuations in atmospheric temperature at a particular altitude because of turbulence and winds. A second, perhaps even more important type of uncertainty in the context of design is however the *epistemic* uncertainty that results from the use of inadequate, incomplete or even erroneous physical models to encapsulate the behaviour of the system.

In this vein, a statistical characterization of the performance of our representative RLV in the presence of uncertainties in some of its key design characteristics has been conducted in order to demonstrate how variability or uncertainty within these characteristics, whether as a result of true physical randomness or deficiencies that are inherent in the modelling approach, can have a very strong impact on the robustness of the final design. In particular, the effect of uncertainties in the material properties used for the TPS, in the predicted characteristics of the atmosphere through which the vehicle descends during its re-entry, and in some of the inherent characteristics of the air-breathing propulsion system are discussed below.

American Institute of Aeronautics and Astronautics

IV.A. Material Properties

Variability in the thermal properties of the materials used to construct the TPS of the vehicle can have a significant impact on the temperature that its surface attains during operation.[1] The combined influence of uncertainties in the TPS surface emissivity ϵ_{tps} (i.e. on the amount of radiative cooling that takes place), specific heat c_{tps}, and conductivity k_{tps} on the thermal response predicted by our TPS model has been investigated using a Monte-Carlo analysis with 1000 optimization runs set up to design a passive thermal insulator for the leading edge of the wings of our representative RLV. The TPS was assumed to be composed from a layer of Reinforced Carbon-Carbon (RCC) insulation material in order to retain the temperature of the underlying structure below 500 K for the duration of the re-entry. A uniform distribution of material properties with a $\pm 20\%$ deviation around their nominal values was adopted in order to characterise the inherent variability in the fabrication of the TPS together with the possibility of thermal degradation and mechanical damage during the previous flight history of the craft. The results of this Monte-Carlo analysis, presented in Fig. 13, shows that this assumption results in a distribution of predicted TPS optimal thicknesses about a nominal value of 96.8 mm (see Fig. 15 on the next page). Statistical analysis (see Fig. 14 on the following page) then suggests that if the assumed variability in material properties is accurate, then designing the system to the predicted nominal TPS thickness would result in higher than nominal heating of the structure of the vehicle on 45% of missions, but that, if a design margin of, say, 110% of nominal was adopted, then the likelihood of the system not meeting its specified performance would be very small indeed. The great advantage of the statistical process is that it allows the safety margins and required design tolerances on the system to be revealed in this way, allowing adequate margins to be incorporated into the design or, alternatively, focusing attention on those elements of the system that need to be better quantified before the design can proceed to fruition.
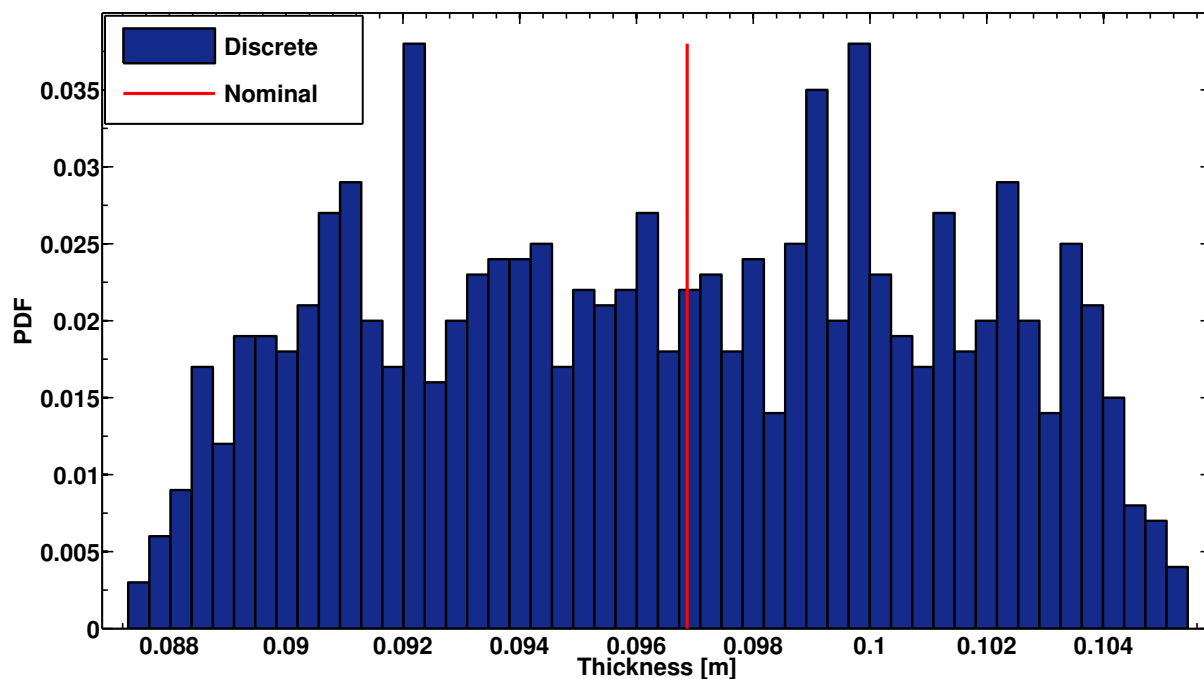

Figure 13: Results of a 1000-sample Monte-Carlo simulation of the performance of the leading edge TPS along the nominal trajectory. The TPS material is assumed to be Reinforced Carbon-Carbon (RCC) with stochastic emissivity $\epsilon = 0.79 \pm 20\%$, specific heat $c_m = 0.770$ kJ/(kg.K)$\pm 20\%$, and conductivity $k_m = 4.3$ W/(m.K)$\pm 20\%$.

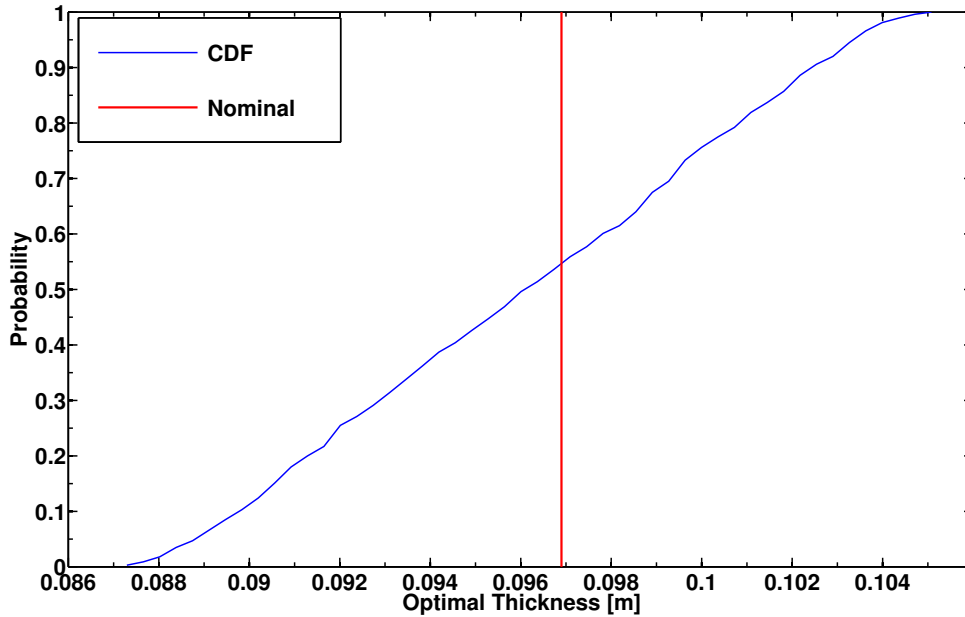American Institute of Aeronautics and Astronautics

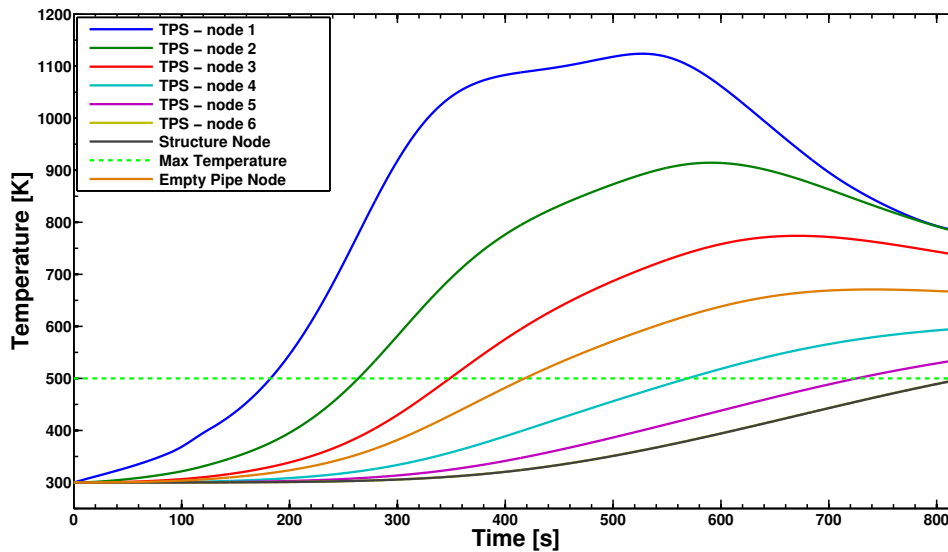**Figure 14:** CDF curve for the optimal TPS thickness.

Figure 15: Thermal performance of a passive TPS with a nominal optimal thickness of about 10 cm.

IV.B.   Active Cooling System

The use of a combination of actively cooled panels in conjunction with a passive TPS has been investigated for the re-entry phase of the mission of our representative RLV. The analysis presented below uses the thermal modelling approach introduced in Section II.D on page 4 to demonstrate the advantages over the use of a passive thermal protection system of adopting an active thermal management system in which the re-circulation of a cryogen, e.g. liquid hydrogen fuel, is used to enhance the efficiency of the TPS in those areas of the vehicle which are most exposed to a severe heating environment (such as at the leading edge of the wings, or at the nose stagnation region), or even to actively cool certain elements of the propulsion system. For present purposes, a simple 'on/off' controller (such as that used in a domestic refrigerator) has

American Institute of Aeronautics and Astronautics

been modelled, allowing the ACS to be switched on or off when the temperature of the underlying structural skin of the vehicle attains a prescribed threshold value. In the results presented here, the skin was assumed to consist of 2 mm thick titanium, and the threshold was set to include a 10% margin below the material's critical temperature (here assumed to be 500 K) to account for thermal inertia within the structure. The mass flow rate of coolant $\dot{m}_{cool}$ was held constant at 5 kg/s when the ACS system was switched on, and the hydraulic diameter of the ACS feeder pipes was set to 5 cm.

A more comprehensive analysis than that presented here would be required in order to evaluate the optimal combination of design parameters that result in the most efficient and lightweight thermal protection system for the vehicle. Similarly, a more sophisticated control system for the flow rate through the system could be adopted in order to reduce the cyclic thermal loads that the present control strategy induces in the structure throughout the duration of the re-entry trajectory. These extensions to the models described here, in particular the use of a more sophisticated control model for the coolant flow rate, would be relatively straightforward to implement, and the results presented here serve thus simply to demonstrate the capabilities of the TPS module within HyFlow.

In designing a simple ACS for the leading edges of the wings which allows straightforward comparison with the performance of an equivalent passive TPS, the example of the previous section was modified by reducing the overall thickness of the RCC layer from its nominal optimal thickness of 96.8 mm to a value of 60 mm, creating two layers of 3 cm-thick RCC, denoted TPS1 and TPS2, one on either side of the ACS feeder lines (see Fig. 3 on page 6: in the present example, node 1 is at the surface of the vehicle, node 2 is within TPS1, node 3 and node 4 are in contact with the coolant pipe lines, node 5 is within TPS2, and node 6 is at the interface between TPS2 and the vehicle structure). As a point of comparison, the performance of the system with the ACS switched off entirely during the descent is depicted in Fig. 16. As can be seen in the figure, the temperature within the structure rises to about 800 K by the end of the descent, and thus the thermal management system, at least when operated in this passive mode, clearly does not meet the design requirement that the temperature of the structure be maintained below 500 K for the duration of the mission.
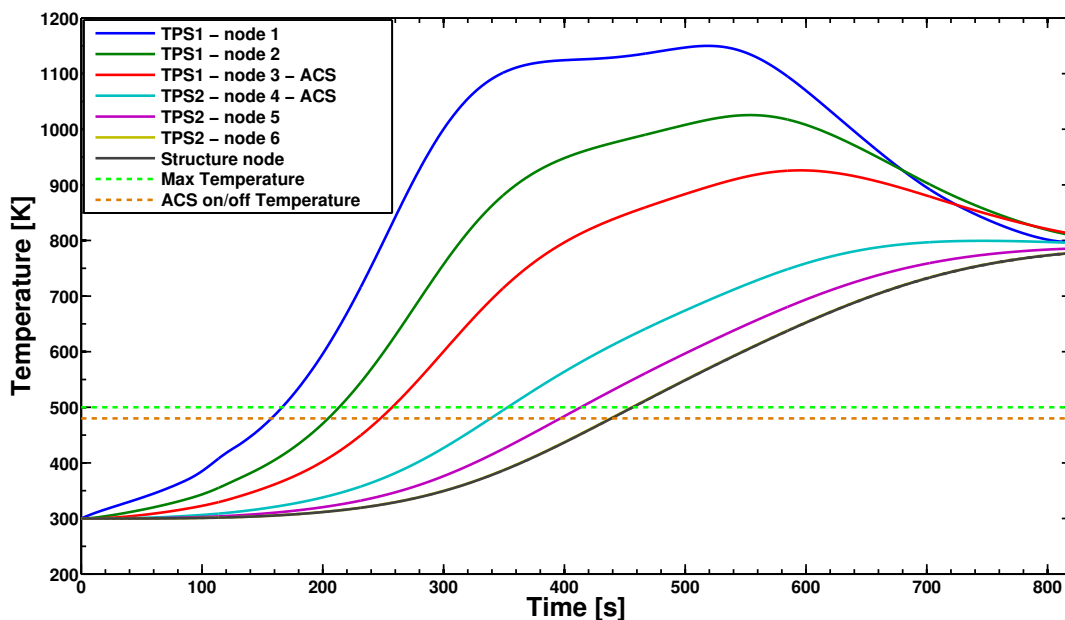

Figure 16: Thermal performance of a passive TPS with a reduced thickness of about 6 cm.

In order to ameliorate the heat load on the underlying structure, the thermal management system is thus run in active mode. The variation of temperature within the TPS when the ACS is allocated a total cryogen volume of 50 m^3 is shown in Fig. 17 on the following page. At the end of a short initial phase during which the system works as a passive TPS, the temperature of the structure becomes high enough to activate the cryogen flow within the ACS. The system responds by maintaining the temperature of the structure below

American Institute of Aeronautics and Astronautics

its critical temperature until a point at about $t = 650$ s into the descent where, due to boil-off, all the cryogen within the tank has been consumed. Thereafter, the TPS continues to act as a passive thermal shield for the remainder of the trajectory. This cooling strategy results in the structural temperature reaching 580 K by the end of the re-entry path. Despite a significant reduction in the temperature of the structure as compared to a fully passive TPS of the same thickness, this system also does not meet the design requirements.
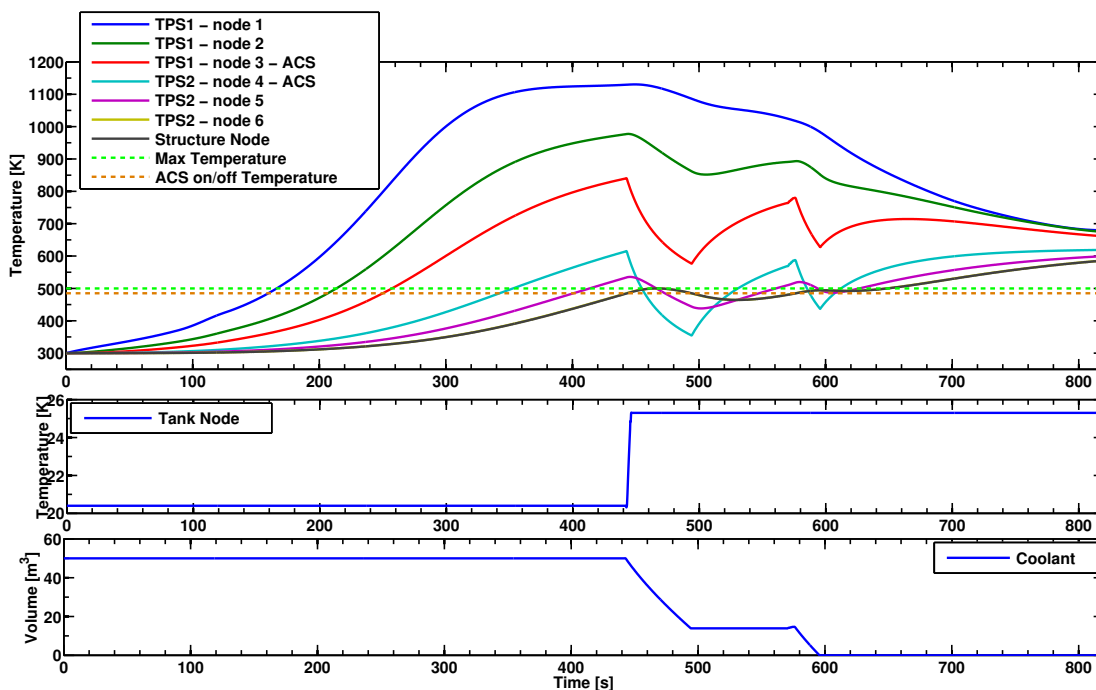

Figure 17: Thermal performance of an Active Cooling System with a coolant reserve of 50m^3.

Figure 18 on the next page shows the behaviour of the same system as before, but when instead 80 m^3 of cryogen is made available to the ACS. In this case, the ACS manages to keep the temperature of the structural skin within the desired limits throughout the duration of the re-entry, even though all the cryogen is still consumed shortly before the end-point of the descent is reached. Despite the simplicity of the thermal management system modelled here, these results illustrate the ability of the TPS module within HyFlow to enable the type of parametric studies and trade-offs between options that would be necessary for the effective and robust multi-disciplinary design optimisation of any future Reusable Launch Vehicle.

IV.C. Ground-hold Analysis

As discussed in Section II.D on page 9, the TPS of the vehicle must be designed not only to protect the vehicle from the thermal loads experienced in flight, but also during those times when the vehicle is being held on the ground prior to a mission and its tanks are full of cryogenic fuel. The danger is that cooling of the structure might result in the build-up of a layer of ice on the outer surface of the vehicle. To model this phenomenon using the thermal module within HyFlow, a 20 metre-long integral tank, containing a volume of 420 m^3 of fuel and located within the forward fuselage of the CFASTT-1 vehicle, was assumed to be insulated using a foam material with a 4 cm thickness. The tank was considered to be directly attached to the load-bearing structural skin of the vehicle, which in turn was assumed to be covered by the same TPS as described in the previous section of this paper (although, for obvious reasons, the active element of the system was switched off for the entire analysis!). The behaviour of the ice layer on the surface of the vehicle during a 2-hour long ground-hold in sea-level ambient conditions was modelled using the approach described in section II.D on page 9. The evolution of the temperature within the tank, its insulation, and the TPS during the ground-hold operation is shown in Fig. 19 on the following page. The temperature in the tank (assumed to contain liquid hydrogen at 20.4 K) is responsible for drawing down the temperature
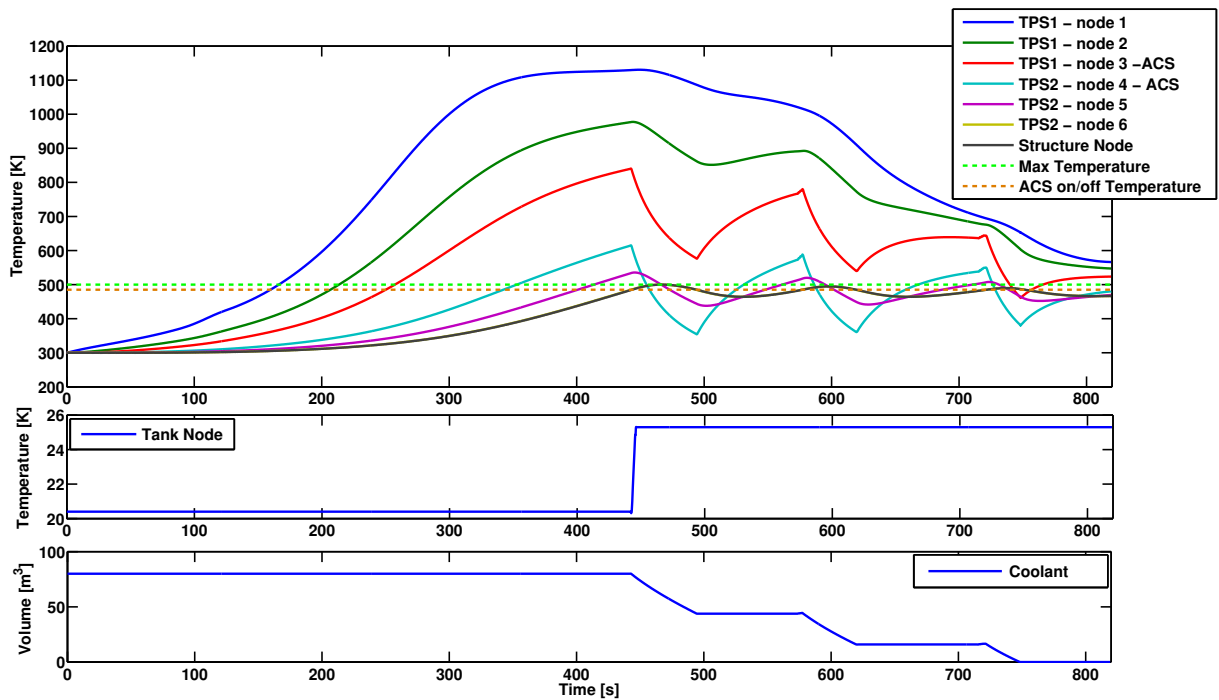
American Institute of Aeronautics and Astronautics

Figure 18: Thermal performance of an Active Cooling System with a coolant reserve of 80m^3.
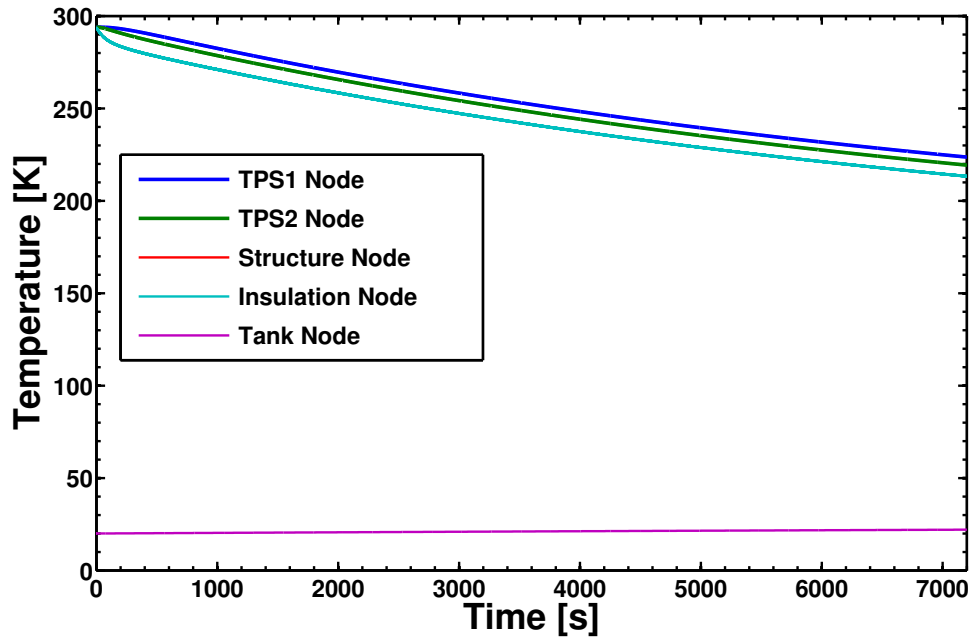

Figure 19: Evolution of the nodal temperatures during ground-hold operations.

within the remainder of the system, to the extent that, at the end of the ground hold, the temperature at the surface of the vehicle reduces from 288 K to 225 K. The associated growth of the layer of ice on the surface vehicle over the duration of the ground hold is shown in Fig. 20 on the next page. As can be seen, the layer of ice appears first at about 28 minutes after the tank has been filled. The total thickness of the layer of ice reaches about 5.5 cm after two hours, amounting to a mass of water attached to the vehicle of
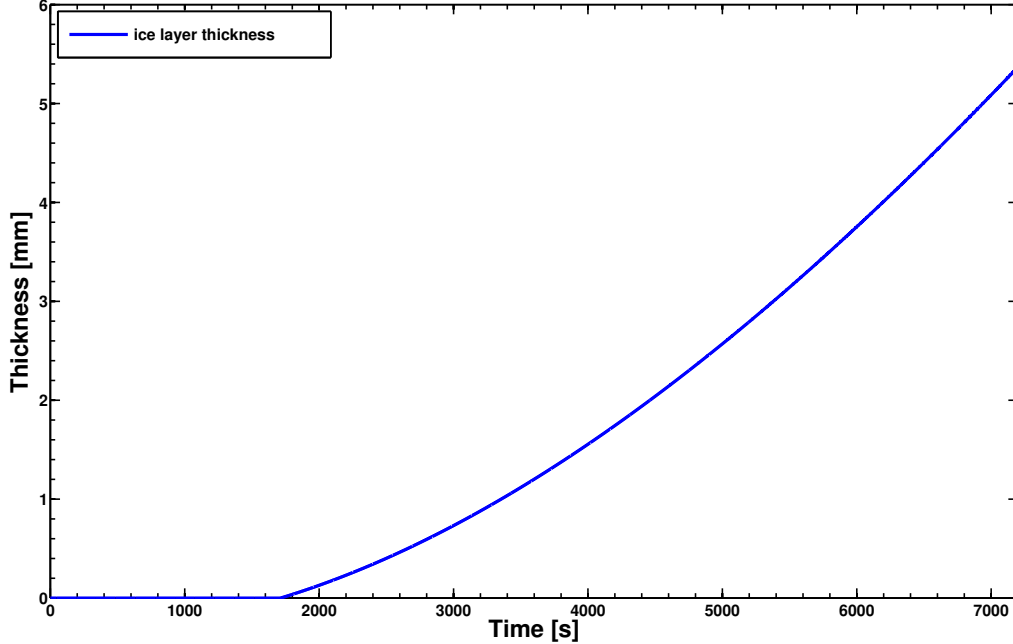
American Institute of Aeronautics and Astronautics

Figure 20: Growth of the ice layer during ground-hold operations.

approximately 55 kg per square metre of surface area covered (this amount of ice could potentially increase the GTOM of the CFASTT-1 vehicle by about 414 kg even if only the forward-fuselage strakes were to be coated). If, instead, the passive TPS considered in section IV.A on page 16 were to cover the vehicle (in other words a system consisting of a 10 cm thick layer of RCC instead of a 6 cm layer) then, as shown in Figs. 21 on the next page and 22 on the following page the ice first begins to appear about 50 minutes after the ground-hold phase has started, and the layer reaches a thickness of only 3 cm (i.e. about 225 kg added to the GTOM of the CFASTT-1 vehicle) after two hours. This comparison reveals a rather interesting mechanism whereby a lightweight, advanced cooling system, designed for maximum in-flight performance, may in fact become somewhat of a liability when the formation of ice during the ground-hold element of the mission is considered. The resolution this conundrum is not entirely apparent as yet - certainly the obvious route of increasing the thickness of the insulating layer between the tank and the structural skin would appear to be at least partially self-defeating.

IV.D.   Atmospheric Model

The natural variation of the thermodynamic properties of the atmosphere about their nominal values is a major source of uncertainty in the prediction of the performance of any trans-atmospheric vehicle. This uncertainty is represented in HyFlow by treating the atmospheric temperature profile, $T_\infty(h)$, where h denotes altitude above sea level, as a random variable. More specifically, if the nominal temperature profile within the atmosphere is denoted as $T_\infty^{nom}(h)$, then a representation of the temperature profile in the presence of uncertainty is constructed as

$$T_\infty(h) = T_\infty^{nom}(h) + \varepsilon(h)S(h) \tag{32}$$

In this expression, ε is an error bound function which captures the statistical variance of the temperature with altitude. This function can, at least in principle, be determined from measurement. For present purposes, and in the absence of better information, ε is modelled very simply by linear interpolation between assumed bounds ε_L and ε_U on the uncertainty at the lower ($h = 0$) and upper ($h = h_U$) edges of the atmosphere, respectively, so that

$$\varepsilon(h) = (1 - h/h_U)\,\varepsilon_L + (h/h_U)\,\varepsilon_U \tag{33}$$

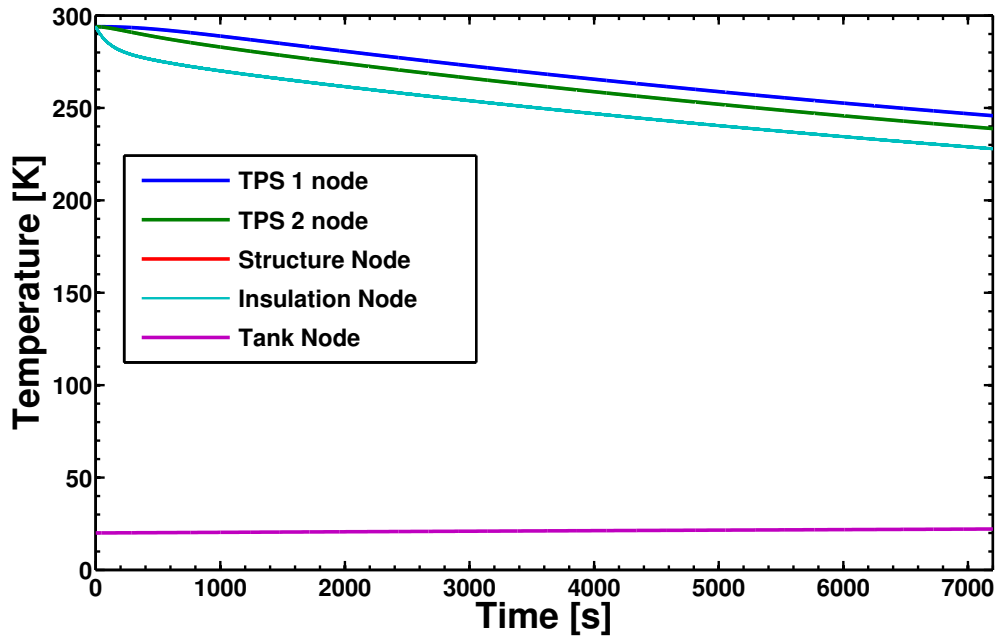American Institute of Aeronautics and Astronautics

Figure 21: Evolution of the nodal temperatures during ground-hold operations for the nominal optimal TPS thickness.
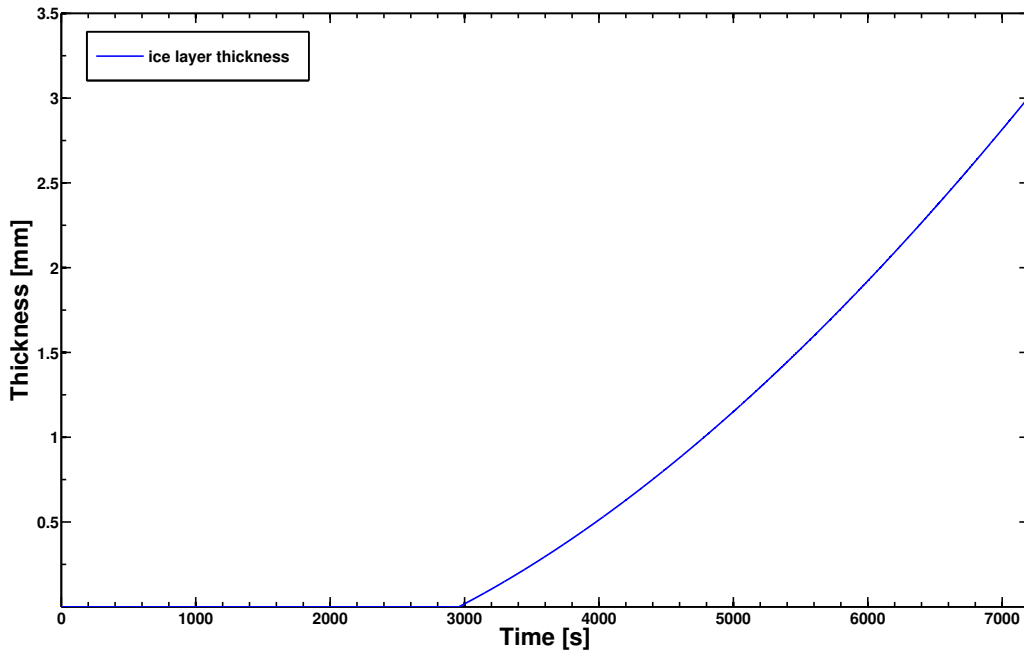

Figure 22: Growth of the ice layer during ground-hold operations for the nominal optimal TPS thickness.

The function $S(h)$ captures the detailed statistical form of the distribution of the temperature perturbations about the nominal variation with altitude. For present purposes it is assumed simply that $S(h)$ is a uniform distribution on the interval $[-1, 1]$. This assumption, although appearing at first sight to be physically rather simplistic, is of great utility when testing the robustness of a design as opposed to when performing

American Institute of Aeronautics and Astronautics

a direct simulation of its likely performance. Finally, the variability that is introduced into the free-stream temperature using this approach are propagated into the remainder of the atmospheric model by imposing the ideal gas law and barostatic equilibrium. A typical variation of the atmospheric properties with altitude generated using this approach is shown in Fig. 23.
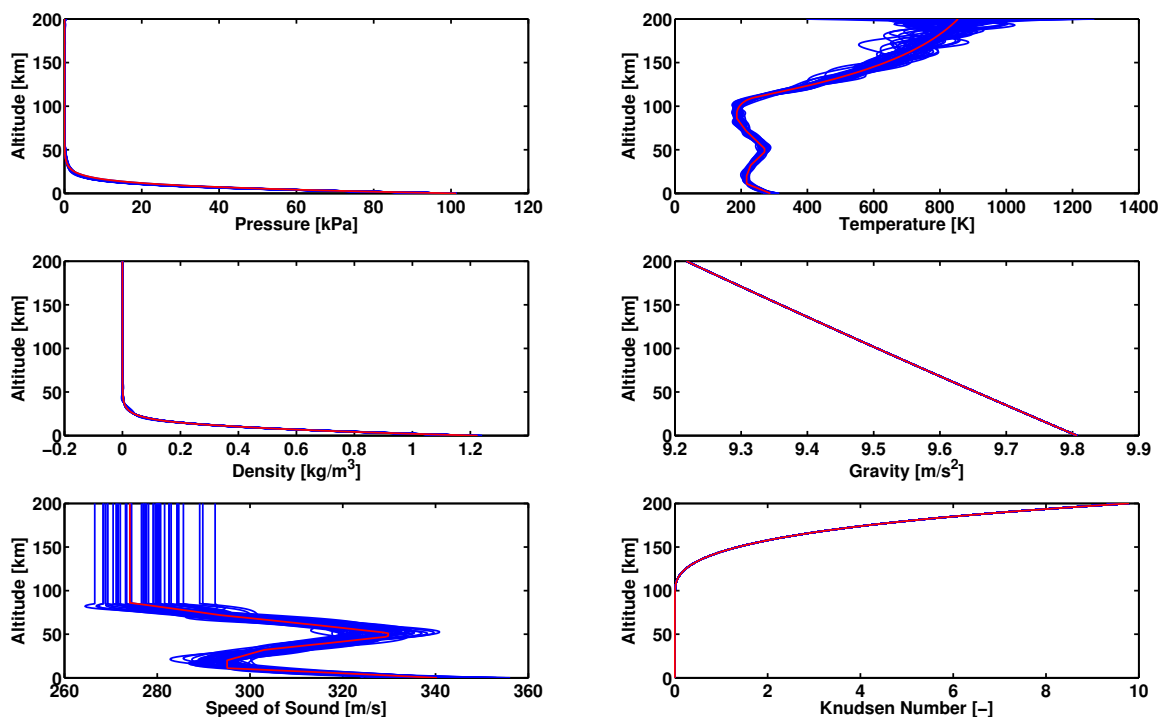

Figure 23: 1976 US Standard Atmosphere subject to uncertainty in the temperature variation with altitude (nominal atmospheric conditions in red). The uncertainty in the atmospheric temperature is taken to vary from 10% of the nominal value (at sea level) to 30% at 200 km altitude.

The sensitivity of the nominal control law to uncertainties within the atmospheric model have been investigated using a set of 10,000 randomized atmospheric profiles in order to perform 10,000 integrations of the re-entry path of the CFASTT-1 vehicle using the baseline control law defined in section III.B on page 14. The distributions of the final states of the vehicle in the presence of variability in the temperature profile within the atmosphere are depicted in Figs. 24, 25, and 26. As sought, none of the re-entry paths meets the nominal conditions (magenta line) when variability in the atmospheric conditions is accounted for. Instead, the final states of the system are dispersed about the nominal, desired, target conditions following a quasi-Gaussian distribution where in general the average values of the final states are lower than the nominal values, but the variance is widely different depending on the variable being considered. For instance, the assumed variability in the atmospheric temperature profile results in a variance of approximately 3 km in the final altitude and 200 m/s in the final speed of the vehicle, which may be of significant concern to the designers, for instance if the vehicle is expected to interface precisely with air traffic management restrictions at the end of its flight. Similarly, the implications of the dispersion of about 1 km in longitude and 55 km in latitude of the final point of the trajectory can only be assessed once the vehicle is placed into its broader operational context, but at least, by adopting the approach that is demonstrated here, the relevant data is available to the designer for analysis. Indeed, the advantage of a statistical approach such as that illustrated here is that it presents the performance characteristics of the vehicle in the form of a likely spread of outcomes, and thus allows an estimate of the variability in the inherent assumptions within the design process, faults in the characterisation of the system, and, indeed, uncertainty in the conditions that might pertain during the operation of the vehicle itself, to be integrated, at preliminary design stage, into a measure of the robustness of the vehicle configuration. The end result is to allow appropriate and realistic margins to be built into the design very early on in its evolution towards a workable prototype.
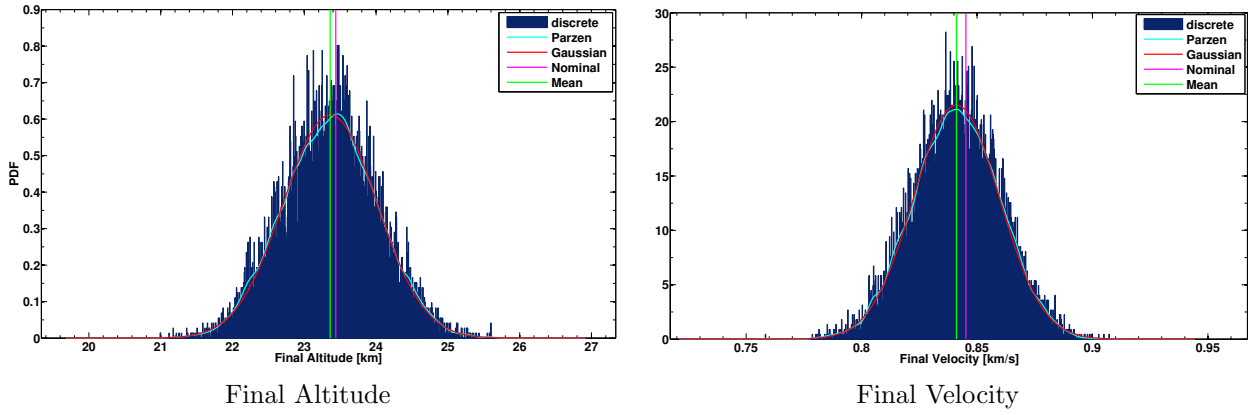
American Institute of Aeronautics and Astronautics

Final Altitude

Final Velocity

Figure 24: PDF of the final states when the nominal schedules of bank angle μ and angle of attack α are integrated using a perturbed atmospheric model.

Final Longitude

Final Latitude

Figure 25: PDF of the final states when the nominal schedules of bank angle μ and angle of attack α are integrated using a perturbed atmospheric model.

Final Flight Path Angle

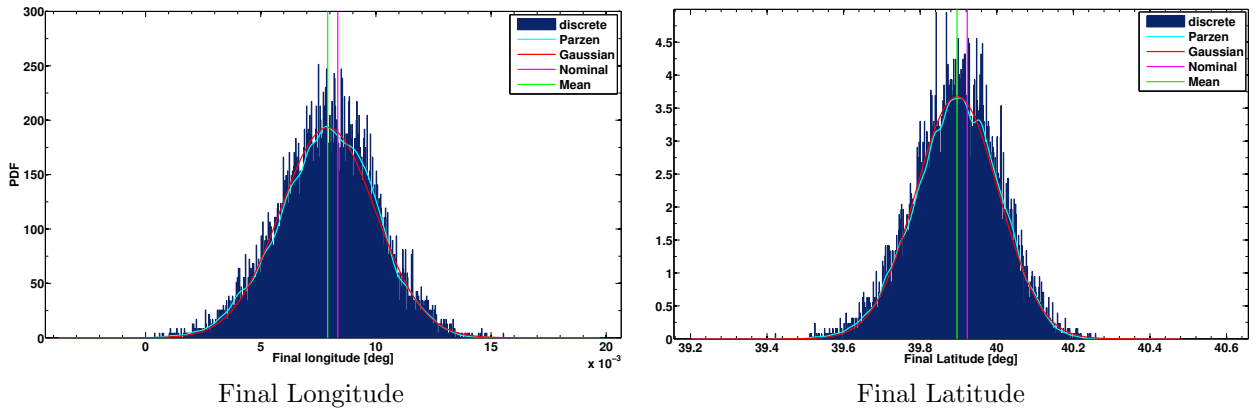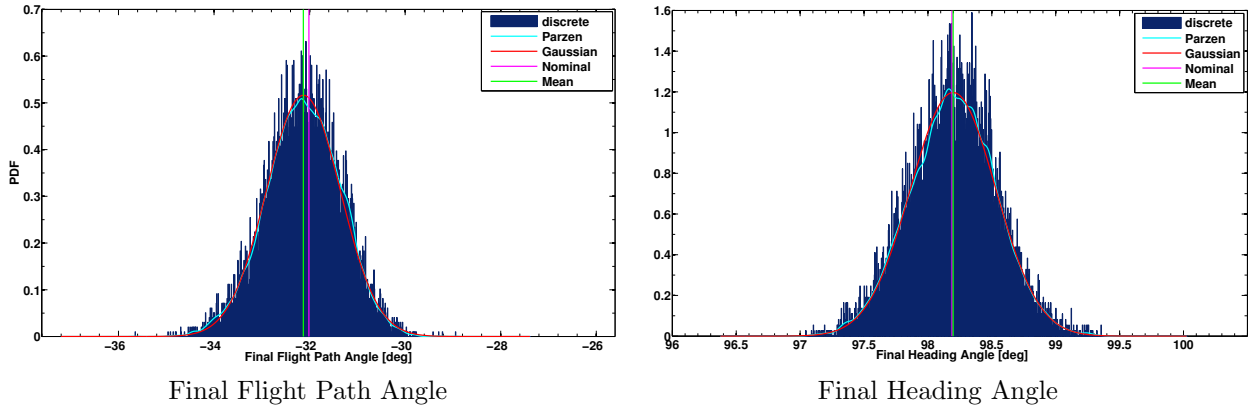Final Heading Angle

Figure 26: PDF of the final states when the nominal schedules of bank angle μ and angle of attack α are integrated using a perturbed atmospheric model.

IV.E. Engine Parameters

Variability in the performance of the engines, and indeed the consequences of the selection of certain key design variables, has a critical impact on the feasibility of the vehicle's ascent trajectory. The effect on the

feasibility of the nominal ascent trajectory, presented in section III on page 13, of varying the mixer efficiency of the engine when in ejector mode, the Mach number at which the system switches from Ejector to Ramjet mode, and the relative size of the rocket and ramjet components of the propulsion system of the vehicle, are presented below.

Figure 27 illustrates the sensitivity of the ascent trajectory to the relative size of the rocket and ramjet components of the propulsion system. The aim of the analysis is to assess the performance of the system under the tradeoff where the propulsion system, at the extremes of the analysis, is either predominantly air-breathing or predominantly rocket-like in its behaviour. The overall size of the engine was thus increased (or decreased) by 30% while the rocket size, and consequently the mass flow rate of its propellant, was correspondingly decreased (or increased) by the same percentage. As can be seen, the adoption of an over-sized ramjet results in a slight gain in final payload mass over the nominal case, but at the expense of extremely poor performance early on in the vehicle's trajectory. In the opposing situation where the rocket is enlarged, the time taken to ascend to orbit is significantly extended, and, as a result of the low effective specific impulse of the propulsion system in this configuration, there is a significant loss in payload performance. Put simply, the undersized ramjet is close to being just a simple rocket, and allows very little advantage to be gained at all from the combined-cycle configuration of the powerplant. In comparison, the over-sized design might, at least at first glance, seem very attractive even in comparison to the baseline configuration. The effect of increasing the size of the engine on the remainder of the vehicle design needs to be borne in mind very clearly, however, particularly given the multi-disciplinary focus of the present study.
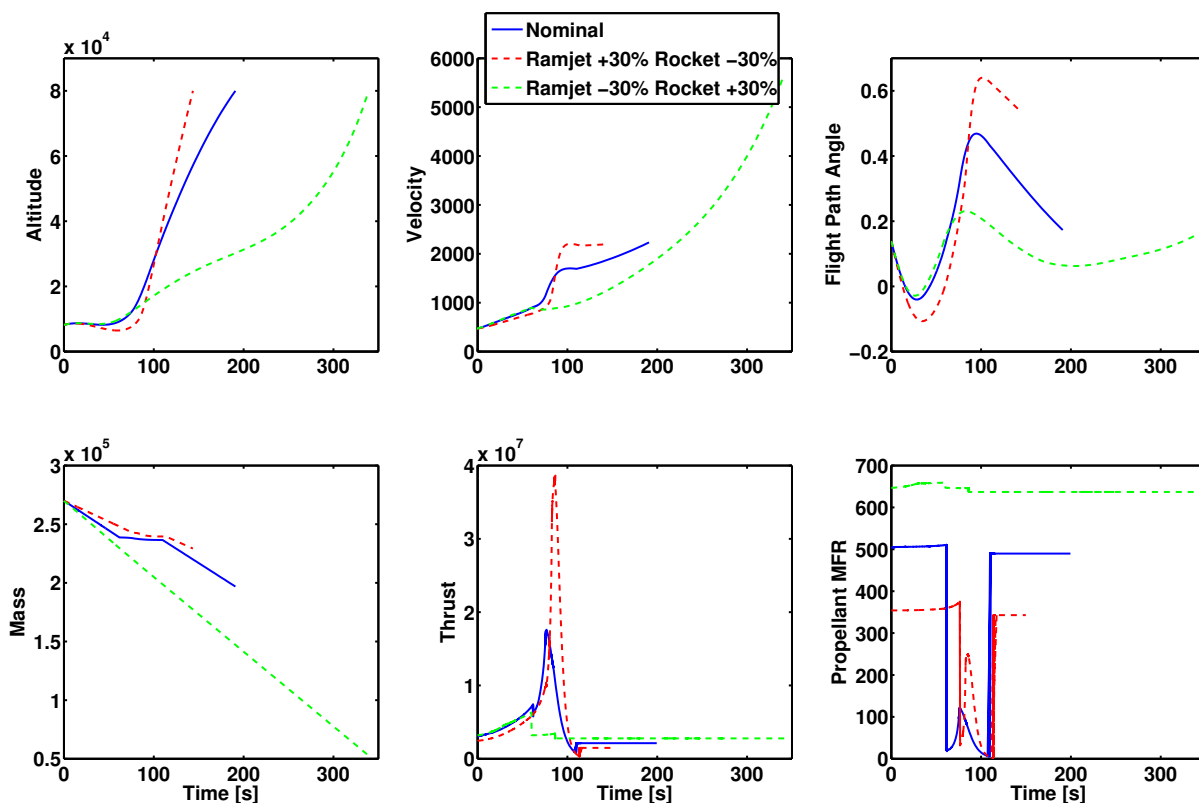

Figure 27: Sensitivity of the ascent trajectory to the relative size of the rocket and ramjet components of the propulsion system.

Figure 28 shows the sensitivity of the vehicle's performance to the efficiency of the mixing between the primary air-flow through the engine and the secondary flow that is induced by the rocket when the engine is operated in ejector mode (see section II.E on page 10). Three off-nominal conditions are considered: two where the mixer efficiency is assumed to be greater than the nominal mixer efficiency of 67% and one condition where the mixer efficiency is taken to be sub-nominal. As is to be expected, the thrust in ejector mode increases as the mixer efficiency is increased, and, as a consequence, the vehicle reaches the Mach

American Institute of Aeronautics and Astronautics

number at which the system switches from ejector to ramjet mode earlier in its ascent. It is also clear however that, with the engine in ejector mode, the vehicle climbs faster the higher its mixer efficiency, with the interesting consequence that the engine when in its subsequent ramjet phase produces a lower thrust, resulting overall in a reduction in the performance of the vehicle. Indeed, a vehicle with too high a mixer efficiency appears to be unable to reach its target altitude; in comparison, the vehicle with mixer efficiency just 15% greater than nominal reaches its 80 km with a small time delay and with a lower final mass than the nominal case. It should be borne in mind however when assessing these results that the calculations presented here were all performed using the same control laws, i.e. those that were established for the nominal trajectory of the vehicle, and that re-optimisation of these laws for the vehicle with its off-nominal propulsion system would most likely allow it to better balance the improved ejector performance with the exploitation of the various operational modes of the engine. It is indeed interesting to note the large reduction in fuel consumption during the ejector phase that results from an improvement in the powerplant's mixer efficiency. It is possible to speculate that this reduction in fuel consumption could be translated into a large gain in payload mass fraction at the end of the ascent simply by employing a set of control laws that are better suited to the engine's operational characteristics. By comparison, the inferences from the data when the mixer efficiency is lower than nominal are much more straightforward: it is clear that the ejector performance in this case is so poor that the transition to Ramjet mode is delayed too late into the ascent for this part of the propulsion system to be effective in accelerating the vehicle up to its orbital speed and altitude.
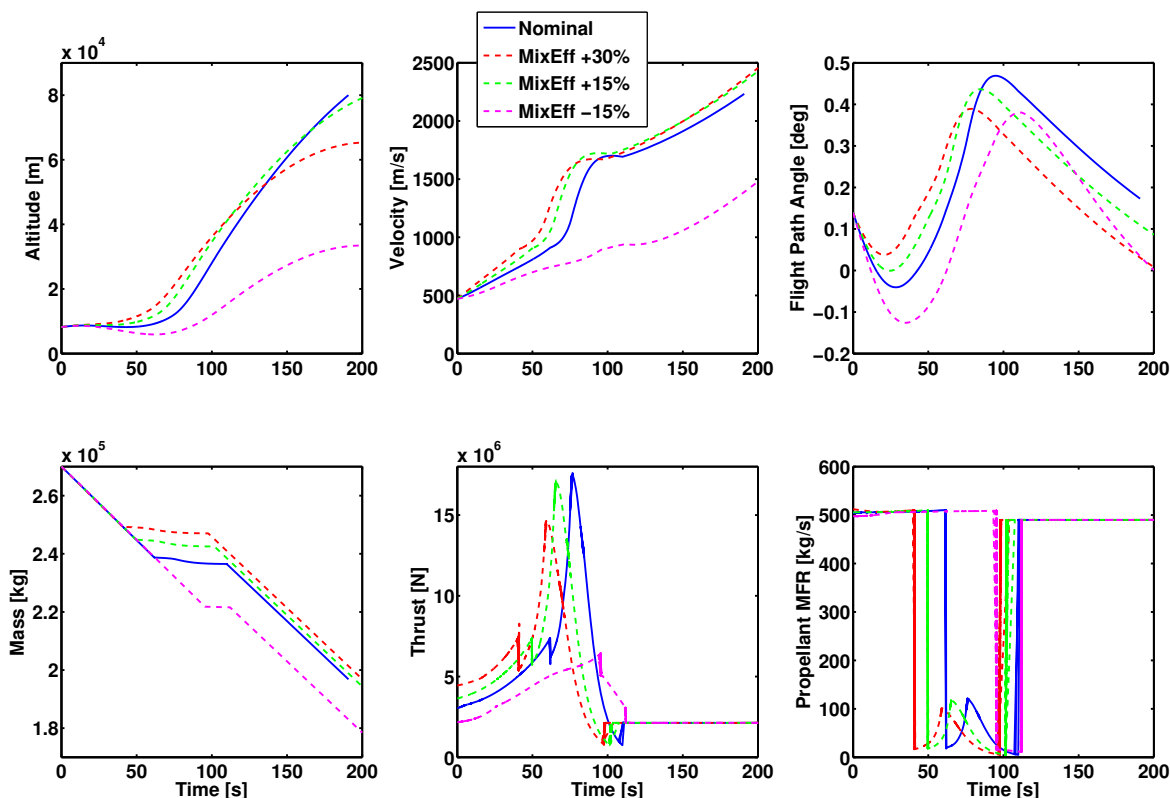

Figure 28: Sensitivity of the ascent trajectory to the mixer efficiency of the engine when in ejector mode.

Finally, Fig. 29 reveals the sensitivity of the system to the Mach number at which the system switches from Ejector to Ramjet mode (see section II.E on page 10). Early switching between these two engine modes can yield significant savings in fuel consumption thanks to the higher specific impulse of the ramjet mode, but can also result in a significant reduction in the thrust produced by the powerplant , and thus the overall impulse given to the vehicle, during the critical mid-phase of its ascent to orbit. Figure 29 shows the clear disadvantage in bringing forward the mode transition to Mach 2.5. In this instance the ramjet is simply not effective enough to continue the vehicle acceleration and thus the speed decreases until the engine switches back to ejector mode. Delaying instead the transition to Mach 3.5 seems to have a beneficial effect on the

American Institute of Aeronautics and Astronautics

vehicle's trajectory: the performance of the propulsion system is better matched at the transition between Ejector and Ramjet modes, as can be inferred from the associated reduction in the size of the discontinuity in the thrust produced by the system at the mode-switch, and the vehicle is able to reach its final target altitude earlier with a slight gain in terms of overall mass to orbit. Although these observations and potentialities all need to be seen in the light of more general considerations of the vehicle's performance and operability, the results presented here again show clearly the benefits of reduced-order modelling in being able to trade and compare various aspects of the performance of the vehicle, and indeed thus to be able to inform early design decisions regarding the key parameters that will govern its eventual configuration.
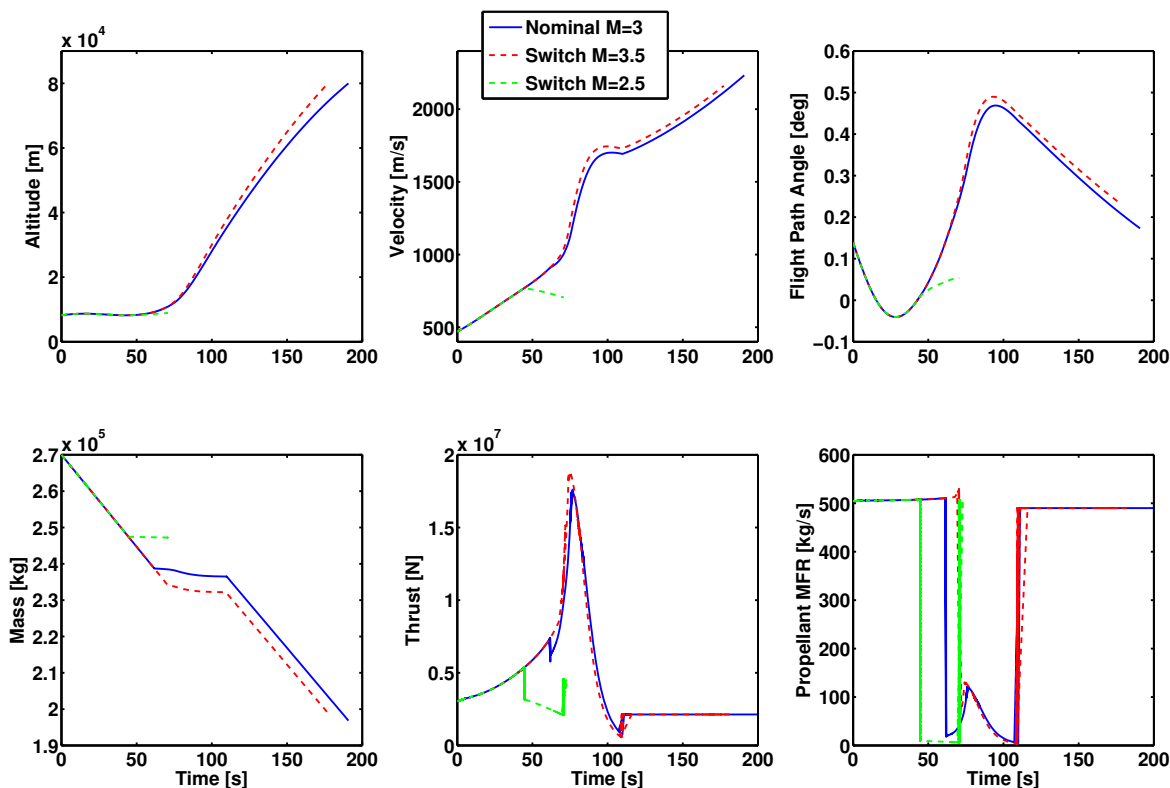

Figure 29: Sensitivity of the ascent trajectory to the Mach number at which the system switches from Ejector to Ramjet mode.

V.   Conclusion

THE present work illustrates the power of reduced-order modelling in examining the sensitivity of the design of a typical reusable launch vehicle to uncertainties and variability in some of its key design parameters. An engineering framework, called HyFlow, has been developed to model some of the complex physics that needs to be considered and properly accounted for in the design of the next generation of RLVs, particularly in terms of their aero-thermodynamic environment, the characteristics of their propulsion systems, and the properties of their thermal protection systems. In this work, various inter-related aspects of the multi-disciplinary design of such a vehicle are explored using this framework. The properties of the thermal protection system that will be required not only to shield the vehicle from the high thermal flux that it will experience both during its ascent into orbit and its subsequent re-entry through the terrestrial atmosphere, but also from the effects of ice formation during ground-hold operations are evaluated in terms of the likely scatter of material properties as a result of manufacturing process and damage and degradation during the life of the vehicle. The advantages of employing an active cooling system rather than a thicker and possibly much heavier passive system are evaluated in terms of the system architecture, the scheduling of the flow

American Institute of Aeronautics and Astronautics

of cryogen through the system, and the amount of fuel that needs to remain in the vehicle's tanks in order to be exploited as an effective coolant during re-entry. Indeed, the sensitivity of the re-entry trajectory to natural variations in the temperature within the atmosphere are also explored, and the statistical scatter of results obtained from a Monte-Carlo simulation of the re-entry in the presence of atmospheric variability allows the design to be evaluated in terms of the permissible margins on its performance, for instance if the vehicle were to be integrated into a tightly-controlled air traffic management system. Certain key design parameters within the hybrid air-breathing propulsion system of the vehicle, particularly the relative sizing of the rocket and ramjet elements of its hybrid configuration, but also the Mach number at which transition between modes is scheduled to take place and the efficiency with which its rocket plume can be mixed with the primary air-flow through the engine, are shown to have critical influence on the success of its mission, and the allowable bounds on these parameters are discussed in the context of our engineering framework. As such, some of the challenges that will be faced by the designers of the next generation of reusable launch vehicles, particularly as they aim to address and overcome the many complications that are introduced into the design and optimisation process through the very tight coupling between the various component systems of the vehicle. Indeed, it is hoped that reduced-order methods like HyFlow will play a significant role in addressing the many conflicting demands on their performance that will need to be successfully balanced in order for these vehicles to eventually become a practical reality.

References

[1] Glass, D.E., Ceramic Matrix Composite (CMC) Thermal Protection Systems (TPS) and Hot Structures for Hypersonic Vehicles, 15th AIAA Space Planes and Hypersonic Systems and Technologies Conference, Dayton OH, 28 April - 1 May 2008.

[2] Anderson, J. D. Jr., Hypersonic and High Temperature Gas Dynamics, McGraw-Hill Book Company, 1989.

[3] Vinh, N. X., Busemann, A., and Culp, R. D., Hypersonic and Planetary Entry Flight Mechanics, University of Michigan Press, Ann Arbor, MI, 1980.

[4] Meador W. E. and Smart, M., Reference Enthalpy Method developed from Solutions of the Boundary Layer Equations, AIAA Journal, Vol. 43, No. 1, 2005, pp. 135-139.

[5] Hamilton, H. H., II, Greene, F. A., and DeJarnette, F. R., Approximate Method for Calculating Heating Rates on Three-Dimensional Vehicles, Journal of Spacecraft and Rockets, Vol. 31, No. 3, 1994, pp. 345-354.

[6] Cohen-Steiner, D., and Morvan, J. M., Restricted Delaunay Triangulations and Normal Cycle, 19th ACM Symposium on Computational Geometry, San Diego CA, 8-10 June 2003.

[7] Bowcutt. K. G., Anderson, D. J., and Capriotti, D., Viscous Optimized Hypersonic Waveriders, 25th AIAA Aerospace Sciences Meeting, Reno NV, 12-15 January 1987.

[8] Wuilbercq, R., Ahmad, A., Scanlon, T., and Brown, R., Towards Robust Aero-thermodynamic Predictions for Re-usable Single-stage to Orbit Vehicles, 18th AIAA/3AF International Space Planes and Hypersonic Systems and Technologies Conference, Tours, France, 24-28 September 2012.

[9] K&K Associates, Thermal Network Modeling Handbook, National Aeronautics and Space Administration, Manned Spacecraft Center, Contract NAS 9-10435.

[10] Harloff, G.J., and Berkowitz, B. M., HASA-Hypersonic Aerospace Sizing Analysis for the Preliminary Design of Aerospace Vehicles, NASA CR-182226, November 1988.

[11] Pescetelli, F., Minisci, E., and Brown, R. E., Re-entry Trajectory Optimization for a SSTO vehicle in the Presence of Atmospheric Uncertainties, 5th European Conference for Aeronautics and Space Science (EUCASS), Munich, Germany, 1-4 July, 2013.

[12] Vasile, M., Finite Elements in Time: a Direct Transcription Method for Optimal Control Problems, AIAA/AAS Astrodynamics Specialist Conference, Toronto, Canada, 2-5 August, 2010.

[13] Pescetelli F., Minisci E., Maddock C., Taylor I., and Brown R.E., Ascent Trajectory Optimisation for a Single-Stage-To-Orbit Vehicle with Hybrid Propulsion. 18th AIAA/3AF International Space Planes and Hypersonic Systems and Technologies Conference, Tours, France, 24-28 September 2012.

[14] Betts, J. T., Practical Methods for Optimal Control and Estimation Using Nonlinear Programming, Second Edition, SIAM, 2010.

[15] Costa, M., and Minisci, E., MOPED: a Multi-Objective Parzen-based Estimation of Distribution algorithm, 2nd international conference on Evolutionary Multi-criterion Optimization, Turin, Italy, 8-11 April, 2003.

[16] Vasile, M., Minisci, E., and Locatelli, M., An Inflationary Differential Evolution Algorithm for Space Trajectory Optimization, IEEE Transactions on Evolutionary Computation, Vol. 15, No. 2, 2011, pp. 267-281.

[17] Mogavero, A., Taylor, I., Brown, R. E., Hybrid Propulsion Parametric and Modular Model: a Novel Engine Analysis Tool Conceived for Design Optimization, 19th AIAA International Space Planes and Hypersonic Systems and Technologies Conference, Atlanta GA, 16-20 June 2014.

[18] Olds, J., and Bradford, J., SCCREAM (Simulated Combined-Cycle Rocket Engine Analysis Module): A Conceptual RBCC Engine Design Tool, 33rd AIAA/ASME/SAE/ASEE Joint Propulsion Conference & Exhibit, Seattle WA, 6-9 July 1997.